A meteorological overview of the ORACLES (ObseRvations of Aerosols above CLouds and their intEractionS) campaign over the southeast Atlantic during 2016-2018: Part 2 – daily and synoptic characteristics

Ju-Mee Ryoo[1,2], Leonhard Pfister[1], Rei Ueyama[1], Paquita Zuidema[3], Robert Wood[4], Ian Chang[5], Jens Redemann[5]

[1] Earth Science Division, NASA Ames Research Center, Moffett Field, CA, USA

10 [2] Science and Technology Corporation, Moffett Field, CA, USA

[3] Department of Atmospheric Sciences, Rosenstiel School, University of Miami, Miami, FL, USA

[4] Department of Atmospheric Sciences, University of Washington, Seattle, WA, USA

[5] School of Meteorology, University of Oklahoma, Norman, OK, USA

15 *Correspondence to:* Ju-Mee Ryoo (ju-mee.ryoo@nasa.gov)

Abstract.

Part 1 provided a climatological overview of the ObsErvation of Aerosols above CLouds and their intEractionS (ORACLES) period and assessed the representativeness of the deployment years. In this Part 2, more detailed meteorological analyses support the interpretation of the airborne measurements for aerosol transport and its interaction with low clouds over the Southeastern (SE) Atlantic Ocean during the September 2016, August 2017, and October 2018 deployments at a daily and synoptic scale.

The key meteorological characteristics *during the September 2016 deployment* are: 1) the southern African easterly jet (AEJ-S), centered at around 600 hPa (~ 4 km), strengthens throughout the month in concert with a warming continental heat low, with the strongest winds occurring around 23 September. These advect both aerosol and moisture in the free troposphere; 2) Mid-tropospheric black carbon (BC) is entrained at times into the boundary layer; 3) Convection over land is dry south of about 10° S, and moist north of 10° S. The daily-mean low-cloud fraction (low-CF) is well correlated with the daily-mean high low-tropospheric stability (LTS, $r = 0.44 – 0.73$ over the flight domain (0-10° E, 5-25° S)), and moderately correlated with the daily-mean boundary layer height (BLH, $r = 0.37 – 0.52$), defined as the altitude of the maximum vertical gradient of moisture. *For the August 2017 deployment, the primary meteorological characteristics* are**:** 1) the AEJ-S is at a lower altitude (~ 3 km, ~700 hPa) and further north (5–7° S) than in September 2016 and only becomes established by 20 August, with a separate easterly jet present aloft above 500 hPa (~ 5.5. km) before that; 2) the mid-tropospheric BC – RH coupling strengthens after the AEJ-S develops, at around 3 km; 3) the daily-mean low-CF is less closely correlated with the daily-mean LTS ($r = 0.16 – 0.57$) and BLH ($r = 0.11 – 0.25$), than in September 2016; 4) Dry convection reaches 700 hPa over the Namibian-Kalahari dryland (~15-25° S, ~18-24° E), generating the moist plume subsequently advected over the southeast Atlantic by the AEJ-S. *For the October 2018 deployment, the key meteorological characteristics* are: 1) the AEJ-S develops around 600 hPa, driven by the Kalahari heat low (~10-25° S, ~12-24° E), but it diminishes over time as moist continental ~~moist~~ convection moves southward; 2) the offshore advection of mid-tropospheric BC (~ 4 km, 600 hPa) ~~, RH,~~ and water vapor are strongly modulated by the AEJ-S around 8-10° S at the early October, but this decreases as mid-latitude frontal systems develop and the AEJ-S weakens around mid--to--late October; 3) the AEJ-S – low-level jet (LLJ) over the coastal Namibian region relationship is the strongest among all deployment months, and the daily-mean low-CF is largely reduced by the strong daily-mean LLJ, especially to the cloud deck's~~sits~~ south; 4) The relationship of the daily-mean low-CF with the daily-mean BLH and LTS are insignificant compared to the other two deployment months, partially due to the variability ~~associated with~~introduced by the passage of the mid-latitude disturbance.

1. Introduction

Smoke aerosols due to Biomass burning (BB) on the African continent play a large role in Earth's climate, both by directly affecting the radiation field and through aerosol interactions with clouds. The smoke is often transported to the

southeast (SE) Atlantic off the west coast of southern Africa, affecting the marine stratocumulus cloud decks radiatively and microphysically. This smoke plume is often observed to be transported along with the moisture from the continent by the mid-tropospheric southern easterly wind (AEJ-S; Adebiyi and Zuidema, 2016; Deaconu et al., 2019; Pistone et al., 2021). Typically, the ocean is the major moisture source region, but this moisture remains in the boundary layer because the strong inversion cap prevents upper movement. Over the southeast Atlantic, free-tropospheric moisture can be laterally transported from the continent, although previous studies do not definitely establish whether the moisture source stems from dry or moist convection. The free troposphere would otherwise be very dry over the ocean over the southeastern Atlantic, because of the large-scale subsidence. For example, the corresponding free troposphere over the SE Pacific, where the Andes mountains prevent the westward transport of moisture from the Amazon, has above-cloud water vapor paths of only one-two mm (Zuidema et al., 2012). Above-cloud water vapor over the SE Atlantic is about twice as large as that over the SE Pacific (Pistone et al., 2021).

These The south Atlantic stratocumulus clouds are also associated with strong large scale subsidence and the anticyclonic circulation associated witharound the semi-permanent St. Helena High over the Atlantic Ocean in the southern hemisphere (SH) (Klein and Hartman, 1993; Wood, 2015). BB aerosols from the fire smoke, because they contain black carbon, absorb shortwave radiation efficiently, so that smoke warms the atmosphere (warming effect), while the low-level stratocumulus clouds reflect sunlight, providing a negative radiative effect (cooling effect). Therefore, depending on how aerosol and low cloud interact, the net radiative effect can be altered. This net radiative effect varies between climate models (Zuidema et al., 2016; Mallet et al., 2021), as the complexity of the interactions is particularly large over the SE Atlantic. Model-observational comparisons reveal large differences (Shinozuka et al., 2020; Doherty et al., 2022).

As a step forward to better understand these aerosol-cloud interaction and their roles in climate, the ObseRvations of Aerosols above CLouds and their intEractionS (ORACLES) project undertook three months of aircraft deployments in September 2016, August 2017, and October 2018 to the SE Atlantic Ocean (flight tracks are shown in Fig. 1a). To better interpret the measurements, we first documented the climatological characteristics during the deployment in part 1 of the meteorological overview paper (Ryoo et al., 2021). Its major conclusions are summarized here: (1) During August 2017, the southern African easterly jet (AEJ-S) was weaker than the climatological mean (2000-2018), largely due to an additional anomalous upper-level jet aloft around $10°$ S. August 2017 was also drier over the SE Atlantic Ocean and the coast (around 0-15° E, 5-10° S) around 700 hPa than climatology, with a stronger low-level jet (LLJ) at 925–950 hPa along the Namibian coast of the SE Atlantic. Consistent with this, the maximum sea level pressure associated with the southern Atlantic anticyclone was stronger and closer to the coast than the August climatological mean (2000-2018). (2) During September 2016, the AEJ-S was comparable to the climatological mean, but the LLJ and the large-scale southern Atlantic anticyclone were stronger than the climatological mean. (3) During October 2018, the AEJ-S was slightly weaker compared to the climatological mean, as were the LLJ and the southern Atlantic anticyclone. October 2018 was wetter over the Benguela coastal region at 600 hPa than the climatological mean. During all the deployment months, sea surface temperatures (SSTs) over the SE Atlantic were warmer

than the SST climatological mean (2002-2018), but the monthly mean low-level cloud fraction (low-CF) was only noticeably lower than the low-cloud climatological mean (2003-2018) in August 2017.

To recap how low-cloud can be associated with aerosol and meteorology, the maps of the climatological monthly mean (2003-2018) are shown in Fig. 1(b, c): the Copernicus Atmosphere Monitoring Service (CAMS) mid-tropospheric (600 hPa) black carbon mixing ratio (BC), European Centre from Medium-Range Weather Forecasts Reanalysis v5 (ERA5) 600 hPa and 925 hPa zonal wind, 800 hPa relative humidity (RH), 800 hPa subsidence, and the low-CF over the deployment region. At a mid-tropospheric level (~ 600 hPa), the BC aerosols from land are modulated by the prevailing mid-tropospheric easterly jet around 600 hPa (~4 km), which is the AEJ-S, propagating into the SE Atlantic Ocean. Pistone et al. (2021) found that pollution indicators, such as carbon monoxide (CO) and aerosol loading, are closely correlated with atmospheric water vapor in the observations, and that both are lofted from the continent and advected by the AEJ-S in September 2016. At lower-tropospheric levels (~ 925-800 hPa), the low clouds reside over the strong coastal low-level jet and the large-scale subsidence regions off of the Namibian coast. These two levels are closely coupled through the mid-level continental anticyclone and large-scale subsidence: the mid-level (~600 hPa, ~4 km) continental anticyclone can return aerosols back to the continent, with subsidence hypothesized to facilitate entrainment of the aerosol into the boundary layer during the month of September (Redemann et al., 2021). The LLJ situated off of the coast of Namibia coupled to the dominant northwestward boundary layer winds further encourage aerosol dispersion throughout the southeast Atlantic marine boundary layer (Christensen et al., 2020; Fig. 1b and c). The microphysical consequences are well observed in the satellite cloud droplet number concentration measurements (Redemann et al., 2021).

Figure 1. (a) ORACLES flight tracks in September 2016 (green ER-2 flight, red for P-3 flight), August 2017 (orange for P-3 flight), and October 2018 (blue for P-3 flight) overlain on a MODIS-Aqua True cloud image and © Google Maps on 13 September 2018. (Figure adapted from Redemann et al., 2021). (b) Map of the September mean (2003-2018) of (a) CAMS 600 hPa black carbon mixing ratio (BC, shading, ppb x 100) overlaid by ERA5 600 hPa zonal wind (black contours, -7, -8, -9 m s^{-1}), 600 hPa horizontal wind vector (magenta, m s^{-1}), and low-cloud fraction (low-CF, green contours, 0.8, 0.9). (c) The same as (a) except for 800 hPa relative humidity (RH, gray hatch as dot, RH > 50, %) overlaid by 800 hPa omega (shading, a positive value is subsidence, hPa day^{-1}), 925 hPa horizontal wind vector (magenta, m s^{-1}), and low-CF (green contours, 0.8, 0.9) over ORACLES deployment region in the SE Atlantic Ocean. The letters represent São Tomé (ST), St. Helena Island (SHI), Ascension Island (AI), and Walvis Bay (WB). CB

115 **stands for Congo Basin (characterized as cool and moist areas) and NKD represents Namibia-Kalahari Dryland (characterized as warm and dry areas). The navy arrow indicates the coupling of aerosol and meteorology in mid- and low-level layers, affecting low cloud decks.**

The sizable stratocumulus deck is reinforced in part by mid-latitude westerlies that are deflected by topography,
120 increasing the low-level tropospheric stability (~~LTS)~~ (LTS) (Richter and Mechoso, 2006). Coupling between meteorology, aerosols, and clouds adds additional complexity (Adebiyi and Zuidema, 2016; 2018). For example, the LTS is modified not only through the surface temperature but also by the absorption of solar radiation by the aerosols residing above the cloud over the ocean (Wilcox, 2010; Sakaeda et al., 2011; Adebiyi et al., 2015; Gordon et al., 2018; Mallet et al., 2019; 2020; Cochrane et al., 2020). Temperature and low clouds can also be affected by the planetary boundary layer structure, but this is also highly
125 modulated by mesoscale- (Hegarty et al., 2018) and synoptic-scale circulation (Liu et al., 2019). The variability in temporal and spatial scales across the different meteorological processes can also influence the aerosol and low clouds differently (De Szoeke et al., 2016; Zuidema et al., 2018; Abel et al., 2020; Scott et al., 2020; Christensen et al., 2020; Zhang and Zuidema, 2021). These all suggest that it is critical to untangle the role of the aerosols on low clouds from the effects of meteorology to identify aerosol-cloud interaction processes.
130 In this Part 2 paper, we provide detailed information on the meteorological conditions affecting the aerosol transport and low clouds at daily to synoptic time scale. In the next section, we discuss the dataset and methodology used in this study. In section 3, we focus on the daily-to-weekly variability of the key meteorological fields during the flight days for each deployment year (September 2016, August 2017, and October 2018). Relationships between low cloud cover and meteorological variables are discussed in section 4 and a summary and conclusions are provided in section 5.

135

2. Data and methodology

The geographic domain of our study region is as shown in Figs. 1(b, c)~~a~~: 30° S–5° N, 20° W–20° E.

2.1. Data

- ERA5 is used to detail the 3-D wind (u, v, ω), temperature, geopotential height (Z), and specific humidity (q) fields
140 (Hersbach et al., 2020). Hourly and monthly data are available on a 0.25 ° longitude x 0.25 ° latitude grid with 37 vertical levels ranging from 1000 hPa to 1 hPa. The ERA5 wind structure compares favorably to that of other reanalysis data such as Modern-Era Retrospective analysis for Research and Applications, Version 2 (MERRA2) and Japanese 55-year Reanalysis (JRA55) over the deployment region (Ryoo et al., 2021).
- The Kalahari heat low (hereafter heat low) is identified by the layer-mean temperature indicated by the difference in
145 geopotential height between 850 hPa and 600 hPa over the Southern African plateau. We apply a threshold value of 2920 m to indicate the spatial extent of the land heat low.

- Lower tropospheric stability (LTS) is defined as the θ difference between 800 and 1000 hPa, to remain below more of the aerosol layer at 700 hPa, following Adebiyi et al. (2015).
- The southern African easterly jet (AEJ-S) is defined by zonal winds (zonal winds < - 6 m s^{-1} (implying easterly winds) around 0-20° E, 5-15° S at a pressure altitude of 600 hPa for September and October, and at 700 hPa for August.
- The Benguela low-level jet (hereafter LLJ; Nicholson et al., 2010) is defined by a 925 hPa horizontal wind speed more than 5 m s^{-1} off the coast of Namibia (0–10° E, 15–25° S).
- Deep, moist convection is defined using brightness temperatures from Meteosat-10 satellite data. Moist convection is defined as brightness temperatures lower than 230 K. The 230K threshold was chosen based on the previous use to indirectly estimate convective rainfall (Ohsawa et al., 2001; Zuidema, 2003)
- The daily (day + night mean) low-CF on 1° longitude x 1° latitude grid is derived from Level 3 Visible Infrared Imaging Radiometer Suite (VIIRS, Hubanks et al., 2019) data onboard the Suomi National Polar-orbiting Partnership (Suomi NPP). The low cloud is defined by cloud-top heights below 2.5 km (Zuidema et al., 2019; Redemann et al., 2021). The monthly-mean low-CF product is derived from the Level 3 Moderate Resolution Imaging Spectroradiometer (MODIS, Platnick et al., 2015a, b) onboard both Terra and Aqua product (1° longitude x 1° latitude grid resolution).
- ECMWF CAMS global reanalysis (EAC4) is the latest global reanalysis dataset of the atmospheric composition produced by the European Centre for Medium-Range Weather Forecasts (ECMWF) (Inness et al., 2019). The CAMS reanalysis assimilates satellite retrievals of total column CO; tropospheric column nitrogen dioxide (NO$_2$); aerosol optical depth (AOD); and total column, partial column, and profile ozone retrievals. The data are available 3-hourly on a 0.75 ° longitude x 0.75 ° latitude grid with 25 pressure levels. CAMS has small biases compared with surface-site observations and the prior Monitoring Atmospheric Composition and Climate (MACC) reanalysis. CAMS reanalysis is also known to be insensitive to cloud cover and satellite overpass time (Witthuhn et al., 2020). That said, an underestimation of CO remains in the boundary layer along with regional bias and under-resolved vertical structure (Inness et al., 2019).

Here we find that the CAMS boundary layer BC mass concentration (900 hPa; ~ 1 km) qualitatively agrees with refractory BC mass concentrations (rBC) derived from a single-particle soot photometer observation over Ascension Island in August 2017 and September 2016 (Zhang and Zuidema, 2019, 2021), with a slight overestimate particularly later in September 2016 (Figs. S9-S10). No comparison was possible for October 2018, but observations from October 2016 and 2017 (Zhang and Zuidema, 2021) confirm the CAMS portrayal of relatively low October concentrations of boundary layer BC.

2.2. Methodology for the decoupled cloud-topped BLH detection

180 The BLH is estimated using 6 hourly ERA5 specific humidity (q) based on a heuristic algorithm we have developed. The computed BLH is designed to include the decoupled cloud-topped planetary boundary layer (PBL) in which the cloud layer is above the well-mixed surface-based layer (See Fig. S1 in the supplementary material). In this quasi-isentropic exchange, the air mass mixing occurs without changing the potential temperature rapidly. This BLH tends to be higher than the height of the well-mixed sub-cloud layer. The methodology for estimating the decoupled cloud-topped BLH is as such:

185 (1) Calculate dq/dz (i.e., a vertical derivative of q, where q is specific humidity [g kg^{-1}], and z is the vertical level [meter]) up to D, the maximum permitted BLH. D is set to 3 km over all the oceanic regions and islands south of 2° N and west of 10° E. D is 6 km over the land (except for the islands).

(2) Find the height at which dq/dz is a minimum at each horizontal grid point in the domains defined in (1).

(3) Find the height where q=10 g kg^{-1} marching downward from height D. We chose q~10 g kg^{-1} as a threshold because this is
190 a reasonable value to indicate influence from the surface. The altitude for where the threshold q is encountered is not sensitive to the threshold value as long as q is not so small (e.g., $q > 4$ g kg^{-1}).

(4) Pick the higher altitude of (2) or (3).

(5) Compute a horizontal average over five points surrounding the point except for the edges.

·   This method indicates consistently decoupled cloud BLH over the SE Atlantic Ocean during the deployments, while
195 small variations in BLH can occur over land when there is local turbulence or convective outflow, reducing the vertical gradient of q.

3. Variability of synoptic-scale circulation during the deployments

3.1 Deployment year 1 (Namibia, September 2016)

The first deployment of ORACLES was based in Walvis Bay (22.96° S, 14.51° E) on the Namibian coast of southwestern
200 Africa. During September 2016, the AEJ-S was comparable to the climatological mean. The LLJ and the large-scale southern Atlantic anticyclone were stronger than the climatological mean. Sea surface temperatures (SST) over the SE Atlantic were warmer than the climatological means, but the monthly mean low-CF was not noticeably lower than climatology in September 2016. Characteristics of synoptic-scale condition and convective features during the September 2016 deployment are summarized in Table 1. Each column in Table 1 represents the dates of occurrence, both ER-2 (Earth Resources 2, NASA's
205 high-altitude airborne science aircraft; NASA ER-2, 2014) and P-3 (NASA's aircraft designed for endurance and range, which is capable of long duration flights; NASA P-3, 2022) flight days, and the longitude-latitude domain for which the synoptic features were captured.

Table 1. Characteristics of synoptic-scale features over SE Atlantic during the September 2016 deployment. The * mark represents both P-3 flight and ER-2 flight were available while +mark represents only ER-2 flight was available. No

 mark represents only P-3 flight was available. MFS represents the mid-latitude frontal system affecting the flight region on that day (x represents no effect).

Dates	Flight days	Lon/Lat domain	MFS	Synoptic description
31 Aug. – 2 Sept.	31 Aug., 2 Sept.	10° W–20° E, 0–20° S	x	Fast-moving oceanic moisture plumes, with the very weak AEJ-S. Strong upper-level and mid-latitude trough intrusion, and cut-off low over 20° W-5° E, 15-30°S were observed, leading to the strong LLJ and southward mid-level flows near the coast. Strong St. Helena High was observed over the central Atlantic (30° W-20° E, 20-45° S).
3–5 Sept.	4 Sept.	10° W–15° E, 0–25° S	4 Sept.	No moisture advection from land along with no AEJ-S signature. Local low-pressure developed over the Namibian coast associated with upper-level disturbance. Strong upper-level and mid-latitude trough intrusion to 20° W-10° E, 20° S, leading to the enhanced southward mid-level flows near the coast. LLJ was perturbed and weakened.
6–9 Sept.	6, 8 Sept.	20° W–15° E, 0–25° S	8 Sept.	Weak moisture advection from land along with the emerging AEJ-S. Strong mid-latitude westerly merging with recirculating flow from land was found near the coast.
10–13 Sept.	10*, 12* Sept.	20° W–20° E, 0–30° S	x	Relatively strong moisture advection from land along with the strengthening of the AEJ-S. The upper-level and mid-latitude trough intrusion, leading to strong LLJ and southward mid-level flows near the coast (0-18° E, 15-30° S), forming local anticyclone associated with high sea level pressure (SLP) over the south of 20° S. The impact of the mid-latitude frontal system was minimal near the coast.
14–17 Sept.	14*, 16+ Sept.	20° W–20° E, 5–30° S	14, 16 Sept.	Fast moisture advection (13 m s^{-1}) from land along with the strong enhancement of AEJ-S. Reduction of LLJ associated with the low-level disturbance. Strong mid-level westerly south of 20° S on 14 Sept. Developing mid-level northward flow associated with an anticyclone and high SLP near the coast on 16 Sept. (0-18° E, 20-30° S). BLH over the SE Atlantic was elevated and disturbed, presumably due to the development of high SLP and strong northward flow on 16 Sept.
18–21 Sept.	18*, 20* Sept.	10° W–10° E, 5–25° S	x	Fast (~8 m s^{-1}) moisture advection along with the developing AEJ-S and emerging LLJ, weak meridional wind and strong mid-latitude westerly jet passing by

				south of 30° S. Low BLH over land and coastal region (0-20° E, 15-30° S) was found both on 18 and 20 Sept.
22–27 Sept.	22+, 24*, 25*, 27* Sept.	10° W–20° E, 5–25° S	24, 25, 27 Sept.	Relatively weak subsidence near the coast of Namibia. Strong AEJ-S. Mid-latitude disturbance associated with the well-developed short waves (upper-level trough-ridge patterns) over the central Atlantic, making the flight regions under the influence of anticyclones and high SLP, especially on 24 Sept. Strong mid-level southward wind and strong LLJ over the flight region of 30° S, 10° W-10° E on 25 Sept. Slightly northward wind near the SE Atlantic (0-10° E, 20-35° S) associated with the mid-latitude frontal system south of 30° S, 0-20° E on 27 Sept.
28–29 Sept.	29+ Sept.	10° W–20° E, 5–25° S	x	Suppressed moisture transport along with the weakening of the AEJ-S, strong meridional wind. Influence of the mid-latitude westerly was minimal due to its migration to the south of 30° S.
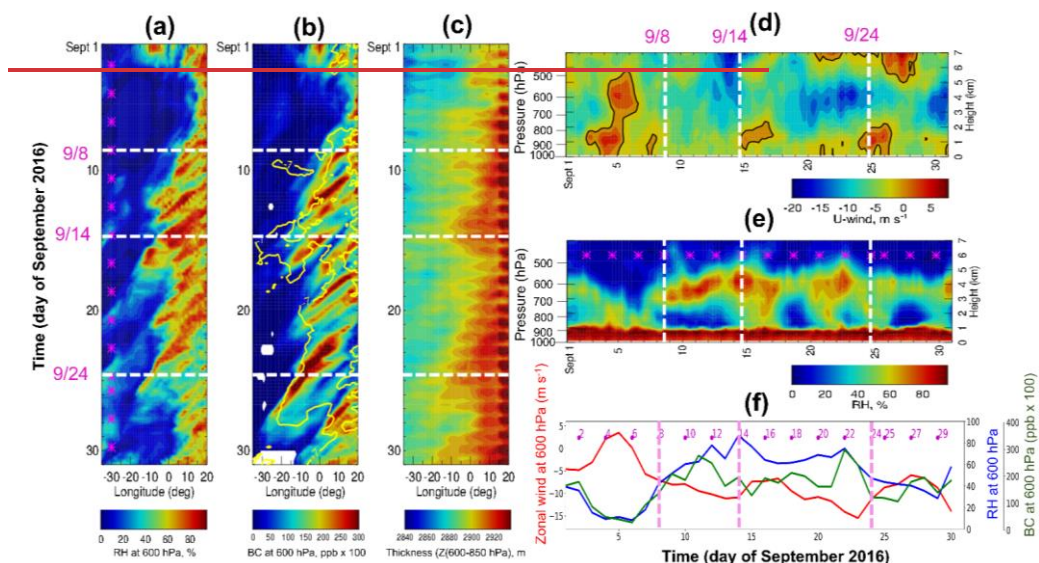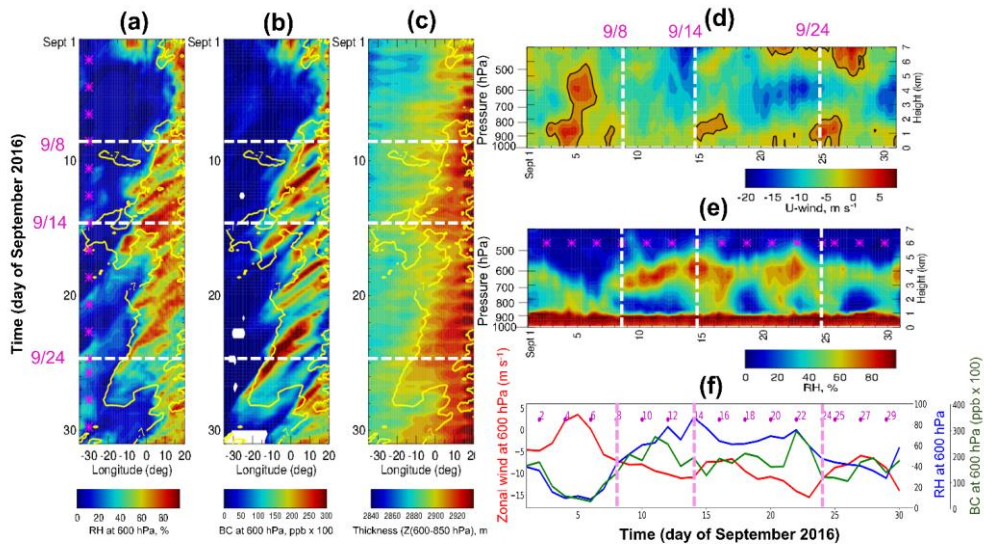
215 **Figure 2. Longitude-time cross-section of 6-hourly (a) 600 hPa RH (%), (b) 600 hPa BC (shading, ppb x 100), and (c) thickness (geopotential height difference (600-850 hPa); high values (> 2920 m) over a South African plateau represents the heat low, m) averaged over 8-10° S during September 2016. (a-c) are overlaid by 600 hPa zonal wind isotach (yellow line, -7 m s⁻¹),. (c) thickness (geopotential height difference (600-850 hPa); high values (> 2920 m) over a South African plateau represents the heat low, m) averaged over 8-10° S during September 2016. (d-e) Altitude-time cross-section of zonal wind and RH at 10° S, averaged over 0–10°**
220 **E during September 2016. The black contour in (d) represents 0 value of zonal wind. (f) Daily time series of the 600 hPa zonal-wind (red line, m s⁻¹), 600 hPa RH (blue line, %), and 600 hPa BC (green line, ppb x 100) averaged over 8–10° S and 0–10° E. The white dashed white lines indicate the flight days investigated further in this study, and the magenta asterisks (and numbers in f) represent the flight days during the September 2016 deployment. White areas in (b) represent the missing data values.**

Figure 2 shows the longitude-time cross-section (i.e., Hovmöller diagrams) of 6-hourly 600 hPa RH, BC, zonal wind, and heat
225 low for September 2016. The AEJ-S is strongly associated with the heat low, consistent with climatology (Ryoo et al., 2021).
The diurnal variations of the heat low are one of the major drivers of the AEJ-S (Fig. S2). Coherent variations of RH and the
AEJ-S suggest the moisture transport from land is facilitated when the AEJ-S extends further west (Figs. 2(a, be); see also
Pistone et al., 2021 for examples). The similar westward transport feature is also shown in water vapor field (Fig. S2). The
AEJ-S strengthening from 8–15 September 2016 between 10° W and 20° E leads the corresponding RH increases by 0–2 days
230 (Figs. 2(a, c, f)).

When the AEJ-S is weak, the transport of RH and BC is also weak, as shown on 5-8 September 2016 (Figs. 2(a, b, f)). The relationship between BC–AEJ-S–RH strengthens as the month evolves, with higher BC mixing ratios occurring when the

AEJ-S gets stronger. Around 24 September, BC mass mixing ratios are high and the AEJ-S is strong, but RH and water vapor (not shown) decrease as they dissipate over the ocean.
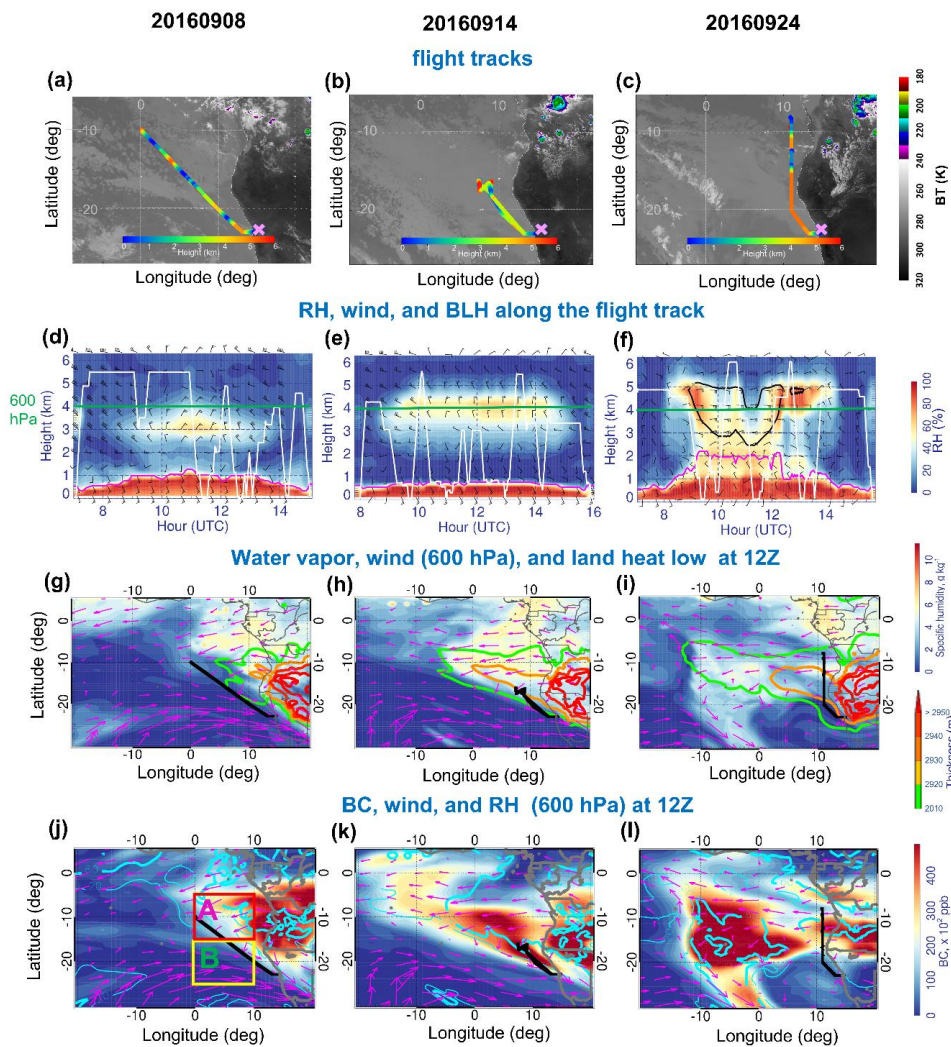
Figure 3. (a–c) The horizontal flight tracks during September 2016 ORACLES deployment plotted on the Meteosat IR 10.8 μm imagery at 13:45 UTC (shading is Brightness Temperature (BT), K). The color of the flight track represents the altitude of the P-3 flight along the horizontal flight track. (d–f) Curtain plot of RH along the P-3 flight track during 8, 14, and 24 September 2016. The white contour represents the flight profile. The magenta line in (d–f) represents the BLH along the flight track. Bold black contours in (d–f) indicate the zonal wind isotach of -8 m s^{-1}. The green line in (d–f) indicates the 600 hPa level. (g – i) Map of 600 hPa specific humidity (q) (color shading, g kg^{-1}) and 600 hPa horizontal winds (vectors, m s^{-1}) overlaid by thickness (thickness: geopotential height (Z) difference between 600 hPa and 850 hPa, color line contour; high values (> 2920 m) over land represents the heat low) at 12:00 UTC on 8, 14, and 24 September 2016, respectively. (j–l) Map of 600 hPa BC (shading, ppb x 100) overlaid by 600 hPa RH (thick cyan line: 60, thin cyan line: 20, %) and 600hPa horizontal winds (vectors, m s^{-1}) at 12:00 UTC 8, 14, and 24 September 2016. The black line in (g-l) represents the horizontal flight track on the given day. The magenta (yellow) box in Fig. 3j refers to region A; 0-10° E, 5-15° S (region B; 0-10° E, 15-25° S).

A focus on three distinct flight days helps illuminate the monthly evolution. 8 and 14 September 2016 were so-called "routine" flight days (Figs. 3(a, b)), designed to build up representative statistics along a fixed track, whereas the targeted flight on 24 September 2016 (Fig. 3c) reached as far north as possible through a coastal African smoke plume (Redemann et al., 2021). The routine flight on 8 September sampled dry conditions with the moist plume located further north of 10° S (e.g., 5–10° S), while the moist plumes with RH ~ 50–60 % in the range of 10–18 kft (~3– 5.5 km) were intercepted by the two other flights (Figs. 3(d–f)). Especially during the 24 September flight, the peak RH lines are aligned with the AEJ-S (black contour, Fig. 3f), where its maximum is observed around 5–10° S, 10–20° E, originating from the continent. Furthermore, on 24 September, high RH is observed throughout the vertical layers from the bottom, indicative of a slightly deeper marine boundary layer compared with the other two highlighted flight days (Figs. 3(d, e, f)).

Both water vapor and BC aerosol are transported by the strong zonal wind (e.g., AEJ-S), but these have different patterns on the different flight days (Figs. 3(g–l)). On 8 September 2016, large moisture and BC gradients over the ocean around 5° W–10° E, 10–20° S are accompanied by a relatively weak zonal wind, with a mid-latitude cyclonic circulation expanding northward up to 20° S (Fig. 4a). On 14 September 2016, a stronger zonal wind transports moisture and BC over the ocean at 10° S, and the jet merges with the subtropical cyclonic circulation evident south of 20° S (Fig. 3hi). By 24 September, as the heat low continues to strengthen, a large-scale mid-level cyclonic circulation becomes established, pushing the westward-moving mid-latitude jet stream further south (not shown). We separated the flight regions into region A and B because of 1) the different relationship of low cloud cover with the meteorological variables between the regions (see also Andersen et al., 2020), and 2) the latitudinal dependency of the LTS and low-cloud (e.g., stratocumulus) fraction (Wood, 2012). The detailed relationship is discussed in the following.
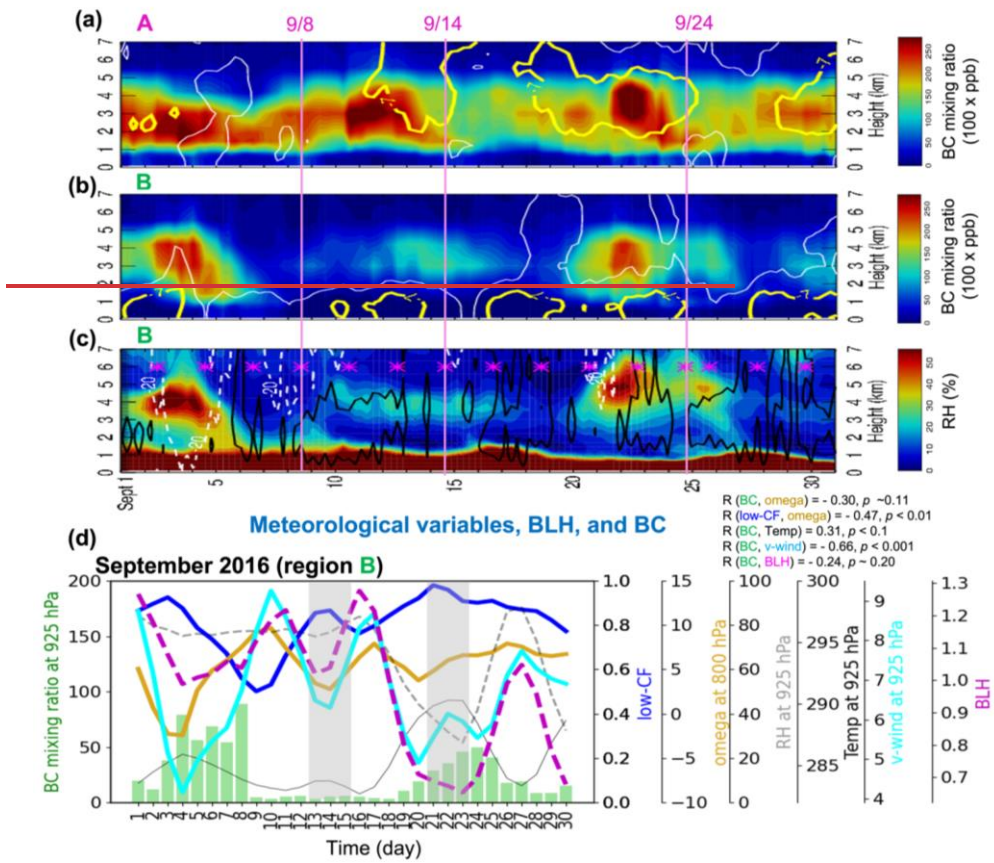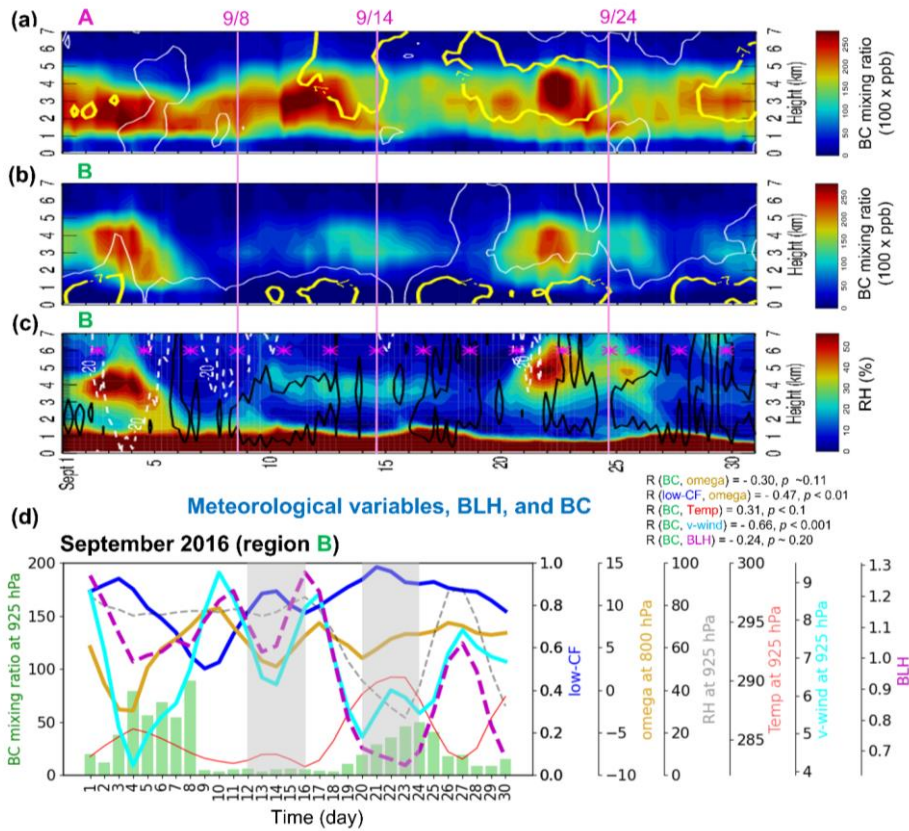
Figure 4. (a–b) Time-altitude cross section of 6-hourly BC (shading, ppb x 100) overlaid by 6-hourly zonal wind isotachs at -7 and 0 m s⁻¹ (thick ~~-~~yellow and thin ~~-~~white lines respectively) averaged over (a) region A (0–10° E, 5–15° S) and (b) region B (0–10° E, 15–25° S) in September 2016. (c) The same as (b) but for 6-hourly RH (shading, %) overlaid by 6-hourly vertical velocities of -20 and 50 hPa day⁻¹ (dashed white ~~dashed~~ and solid black ~~solid~~ lines respectively; positive values represent subsidence) averaged over region B. (d) Time series of daily-mean 925 hPa BC (green bar, ppb x 100), 800 hPa vertical velocity (omega, ω) (gold line, hPa day⁻¹), 925 hPa RH (~~gray~~dashed gray line, %), 925hPa temperature (~~black~~solid red line, K), 925 hPa meridional wind (~~cyan~~solid cyan line, m s⁻¹), BLH (dashed magenta ~~dashed~~line, km), and low-CF (blue line) over region B. Each color line represents the 3-day running

mean. The asterisk in (c) represents the September 2016 flight days. The pink solid lines in (a–c) refer to the three flight days. The light gray shadings in (d) represent the two periods having different BC-RH conditions.

Figure 4 shows the time evolution of BC aerosol, wind, RH, and the cloud deck. For most of September 2016, the low-CF is
280   modulated by the synoptic-scale atmospheric circulation including frontal passages. The width and the intensity of the developing cyclonic circulation shape the moisture and aerosol transport, as well as low-CF (Figs. 3j – l). The AEJ-S (wind at 600 hPa over region A) and the LLJ (wind at 925 hPa over region B) is weakly ~~if insignificantly~~ correlated in September 2016 – (Pearson correlation (R) = 0.32 with *p*-value ~ 0.11; see Fig. S3 in the supplementary material). On some days, the marine boundary layer also contains BC, such as from September 21-24 over region B. HYSPLIT back trajectories and the ~~The~~ aerosol
285   forecasts used during the deployment indicate ~~this~~ the boundary layer BC ~~observed in the boundary layer~~ is aerosol advected directly westward off of the continent that has not reached the altitude of the AEJ-S~~)~~, residing near the boundary layer top (Dobracki et al., 2022), where it can be more easily entrained even when the subsidence is weak (not shown).

      Aircraft observations do not show BC in the boundary layer for most of September (Shinozuka et al., 2020) except on 31 August 2016 (Diamond et al., 2018), indicating the CAMS reanalysis allows for too much entrainment into the boundary
290   layer (reaching 0.8 ppb at times). Simultaneously, the temperature increases and the RH decreases (Fig. 4d). The temperature increase is large enough to suggest the cause is advection from land, but this is not pursued further. The low-CF is not much affected although a slight decrease is found around 23 September. Similar features are also found in region A (not shown).
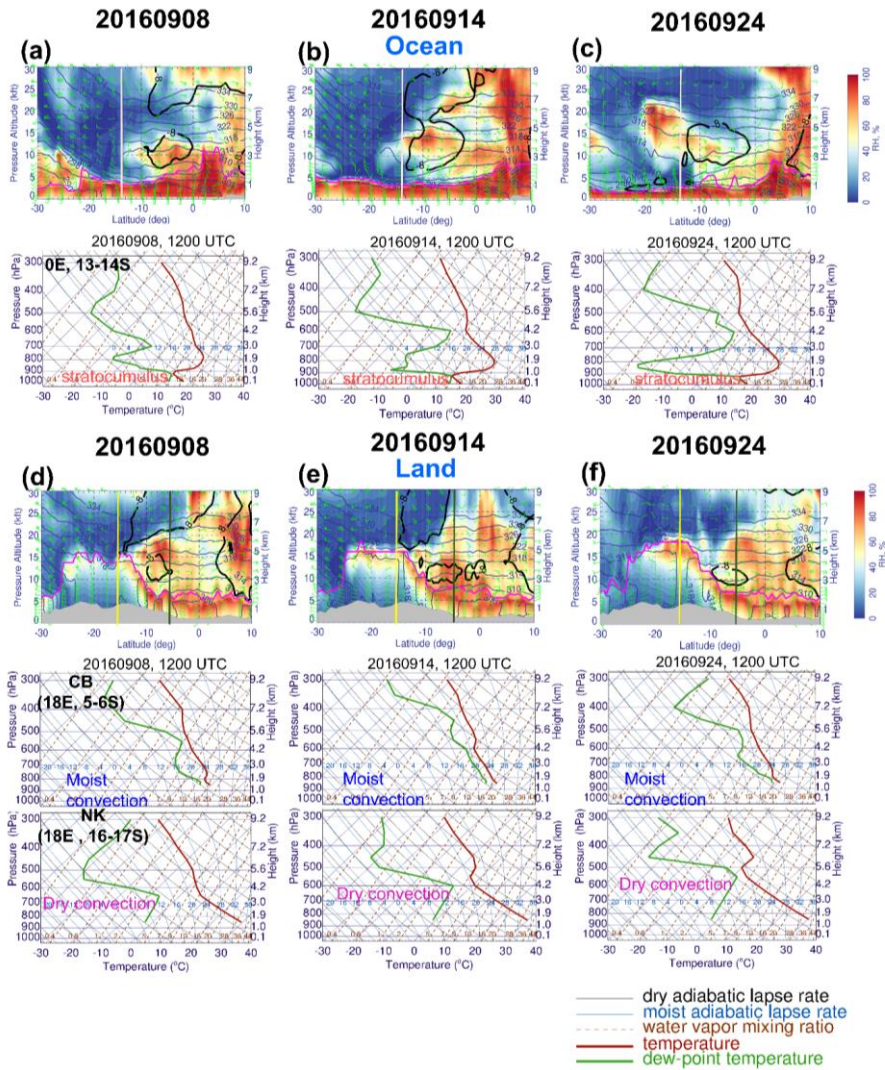
Figure 5. (a–c) *Ocean*: latitudinal cross-section of RH (shading, %), horizontal winds (wind barbs, green, m s⁻¹), θ (navy, K), and
BLH (magenta, m) at 0° E (top) and Skew-T log-P diagram averaged over 0° E and 13–14° S (bottom: from the left) at 12:00 UTC

300   Whether convection is dry or moist can modulate how transported aerosols and moisture interact with clouds (Tao et al., 2012). To differentiate dry from moist convection, soundings and longitudinal cross-sections of RH, winds, and θ over the ocean and the land are shown in Fig. 5. Over the ocean, the oceanic soundings show that the air is saturated when the temperature is equal to dew point temperature (Alduchov and Eskridge,1996) at around 900 hPa (Figs. 5(a–c)), forming stratocumulus. Moisture transported from the continent by the AEJ-S near 600 hPa can lead to occasional saturation, producing scattered mid-level

305   clouds (Adebiyi et al., 2020). In the example of 24 September, the moist plume above stratocumulus resembles a "dry convection" type layer (above 700 hPa). This is indicated by 1) dew point temperature following a nearly constant water vapor mixing ratio line and 2) air temperature roughly following the dry adiabatic lapse rate. This demonstrates that the dry convective layer propagates out from land into the ocean (sounding plot of Figs. 5 (c, e)).

       Over the land, dry convection is more evident south of 10° S. The dewpoint nears saturation, ultimately favoring high RH

310   but ~~still remaining dry~~with insufficient moisture for rainfall below 600 hPa, ~~indicating the formation of dry convection.~~ (Figs. 5(d–f)). ~~There is insufficient moisture for rainfall, but~~ RH ~~reaches higher than~~can exceed 60% and thin mid-level clouds can form at times near the top of the dry convection (Adebiyi et al., 2020). Dry convection over the Namibian-Kalahari dryland (16–17° S) can reach up to 500 hPa (~5.5 km), especially on 24 September (Fig. 5f). This dry convection results in near-saturated conditions at the top of the deep continental boundary layer, explaining the moist plume that is transported westward

315   by the AEJ-S at or north of the dry convection region. In contrast, moist convection is dominant north of 10° S (upper panels (18° E, 5–6° S (CB)) of Figs. 5(d–f)). All soundings over land around 5-6° S have significant ~~energy available for convection (~~Convective Available Potential Energy (CAPE~~)~~). For all cases, the moisture plume around 600 hPa over the ocean is ~~originating~~ transported westward from land by the AEJ-S. although moisture can potentially be also ~~come~~ modulated from a southern mid-latitude disturbance as well (e.g., 31 August 2016; Adebiyi ~~et al~~and Zuidema~~.~~, 2018; Kuete et al., 2021; Ryoo et

320   al., 2021).
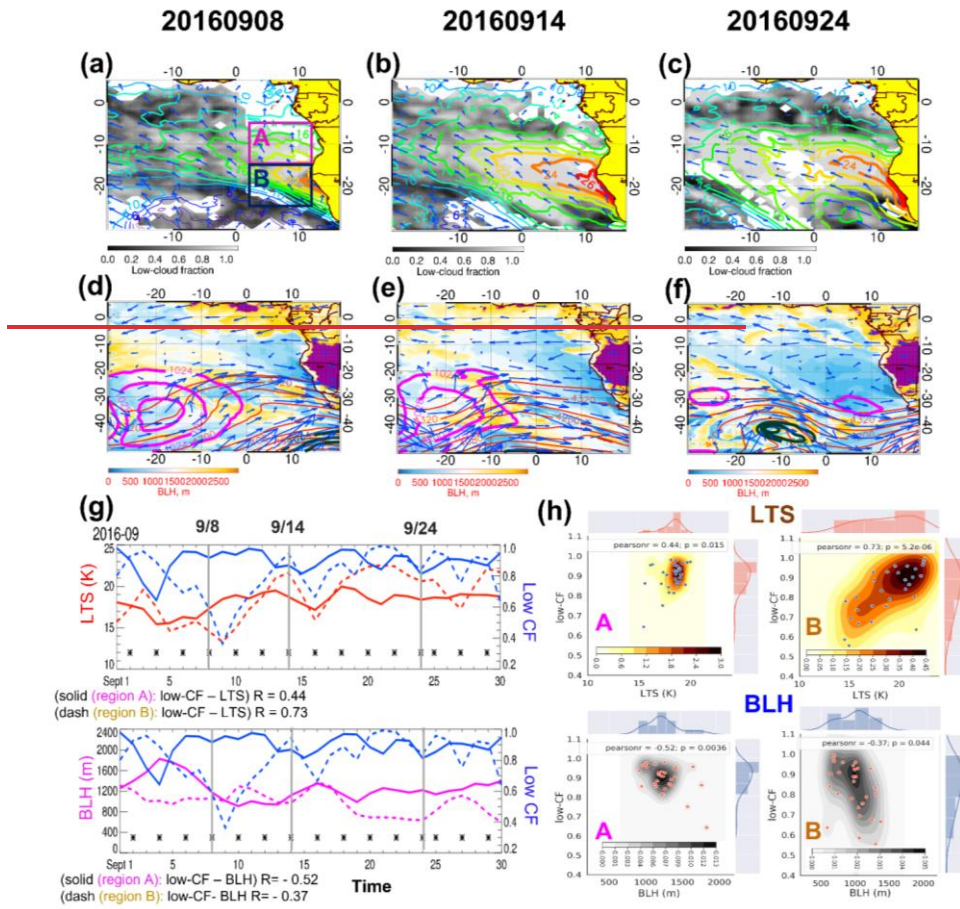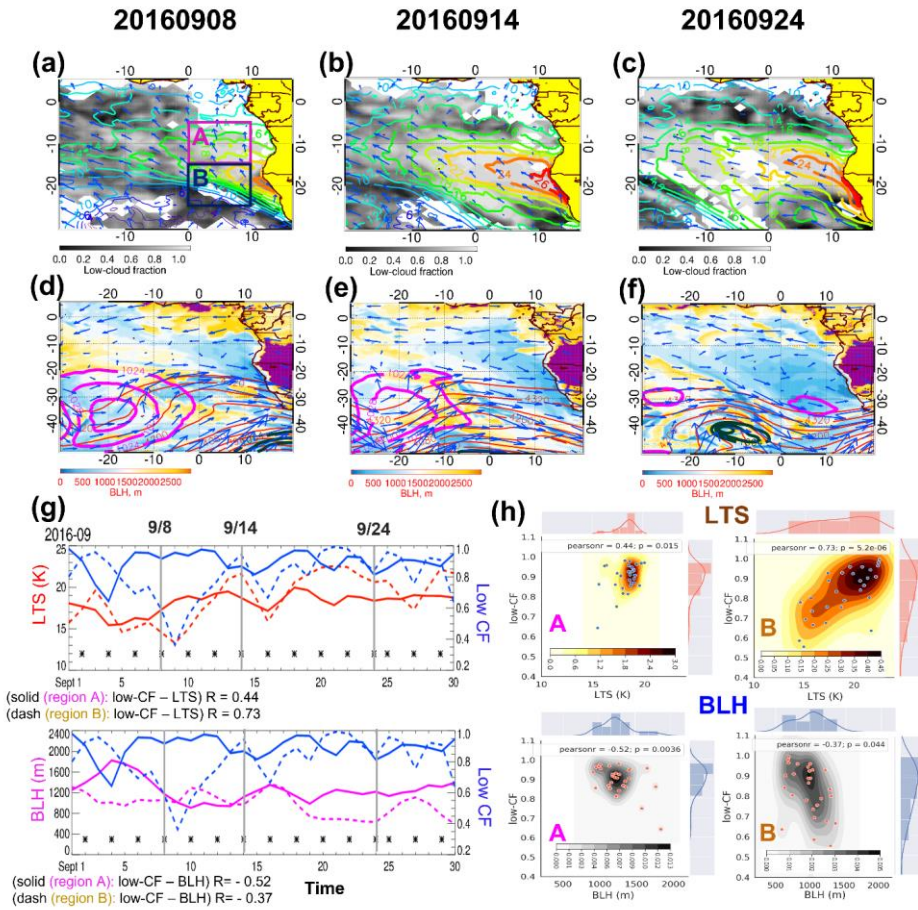
Figure 6. Map of (a–c) daily mean low-CF (shading) overlaid by LTS (contour, K) and 925 hPa horizontal winds (vectors, m s^{-1}), (d–f) BLH (shading, m) overlaid by 600 hPa horizontal winds (vectors, m s^{-1}), 600 hPa geopotential height (red lines, m), and sea level pressure (SLP; dark green (low-pressure: 996, 1000, 1004), and magenta (high-pressure: 1024, 1028, 1032) lines, hPa) at 12:00 UTC 8, 14, and 24 September 2016. (g) (Top) time series of daily mean low-CF (blue lines) and daily mean LTS (red lines, K), and (bottom) daily mean low-CF (blue line) and daily mean BLH (magenta lines, m) averaged over region A (0–10° E, 5–15° S; solid lines) and

region B (0–10° E, 15–25° S; dashed lines) during September 2016. All flight days (8, 14, and 24 September 2016) are marked by asterisk (gray vertical lines). The purple shading over the land in (d–f) refers to BLH higher than 3250 m. (h) The 2-D joint pdf (shading) with scatter plot are shown with 1-D histogram (pdf in line) of (top) daily mean low-CF and LTS and (bottom) daily mean low-CF and BLH over region A (left) and B (right) during September 2016. The solid line in (a) indicates region A (magenta box) and region B (navy box), respectively. The pearsonr in (h) refers to Pearson's correlation coefficient with its statistical significance (*p-value*).

Low cloud structure and cover are influenced by the large-scale subsidence, LTS, and BLH (Klein and Hartman, 1993; Wood 2015), but these relationships will be weaker at synoptic time scales (De Szoeke et al., 2016) compared to the monthly mean variations detailed on Ryoo et al. (2021) and in the complex SE Atlantic environment (Adebiyi et al.and Zuidema, 2018). Here we examine the daily variability of the low-CF over the course of three flight days in Fig.6. Clearly shown is that LTS and low-CF are spatially and temporally positively correlated (Figs. 6(a–c), g). For example, on 14 and 24 September 2016, as the LTS is stronger, low-CF increases over most of the regions. However, on 8 September 2016, a mid-latitude weather system has broken up the sheet of low clouds to the south of 20° S (Adebiyi and Zuidema, 2018), possibly reducing the regional low-CF and lowering the LTS compared to other days (Fig. 4a). Deeper BLHs tend to have reduced low-CF, consistent with entrainment drying. Depressed BLH (< 1 km) promotes the occurrence of a high low-CF as seen on 24 September 2016 (Figs. 6(b, c, f, h)).

Passage of a developing frontal system, indicated by the mid-level (e.g., 600 hPa) trough located on the west of the sea-level low pressure, alters the regional circulation, as shown for 8 and 24 September 2016 (Fig. 6f). This is also indicated by the largely different angle between the 600 hPa wind vectors and geopotential lines (Figs. 6(d-f)), more apparent when low pressure develops south of 30° S. The divergence of the ageostrophic wind links the low-, mid-, and upper-level flow, through the strong vertical motion (Holton, 2004), aiding anomalous ascent at the southern edge of the stratocumulus deck, cooling the lower free troposphere, reducing LTS, and ultimately decreasing the low-CF (Adebiyi et al.,and Zuidema, 2018). The LTS – low-CF relationship is stronger further south (region B, R ~ 0.73) than in region A for this region. Fig. S13 contains further information on the mid-level flow and SLP patterns on all September 2016 flight days. No sensitivity in the result was found either using mid-level (e.g., 600 hPa) and upper-level (e.g., 500 hPa) geopotential height and wind to investigate the development and impact of the mid-latitude frontal system (not shown). The LTS – low-CF relationships are weaker near the coast (e.g., 0–10° E, 5–15° S, region A) compared to further west (e.g., 10° W–0, 5–15° S) for all the deployment months.

3.2 Deployment year 2 (São Tomè, August 2017)

The second deployment occurred in São Tomé (0.34° N, 6.73° E). August marks the transition from austral winter (July) to austral spring (September), as the southern hemisphere warms, and the Kalahari heat low develops. During August 2017, the heat low development was delayed relative to the climatological mean (2000-2018). The August 2017 AEJ-S was weaker than

in climatology due to an anomalous upper-level disturbance (wave) at around 10° S. The August 2017 lower free troposphere (~700 hPa) was also drier over the SE Atlantic Ocean and the coast (around 0-15° E, 5-10° S) than in climatology, with a stronger LLJ at 925–950 hPa along the Namibian coast. Consistent with this, the southern Atlantic anticyclone was stronger and closer to the coast than the August climatological mean. The monthly mean low-CF was noticeably lower than climatology in August 2017 and linked to a warm SST anomaly (Ryoo et al., 2021). The characteristics of synoptic-scale features during the flight days in August 2017 deployment are summarized in Table 2.

Table 2. Characteristics of synoptic-scale features over SE Atlantic during the August 2017 deployment. P-3 flights were available in August 2017. MFS represents the mid-latitude frontal system affecting the flight region on that day (x represents no effect).

Dates	Flight days	Lon/Lat domain	MFS	Synoptic description
5–13 Aug.	9, 12, 13 Aug.	10° W – 20° E, 0–30° S	12, 13 Aug.	Slow, unorganized moisture advection by the relatively slow-moving, weak AEJ-S. Strong cut-off low (20° W, 30° S) disturbed the flow over the west of the flight region on 12 Aug. High SLP developed south of 20° S, 10° W-10° E.
14–18 Aug.	15, 17, 18 Aug.	30° W– 20° E, 0–30° S	15 Aug.	Suppressed AEJ-S, dry condition persisted over flight regions. Mid-latitude trough intruded over the west (20° W-0) of the flight regions, and strong anticyclones associated with high SLP developed over the flight regions. Westerly and southwesterly was intensified along with the anticyclones around 25-30° S, 10° W-10° E.
19–22 Aug.	19, 21 Aug.	30° W– 20° E, 5–25° S	21 Aug.	Strong moisture advection from land, along with the strengthening of the AEJ-S. Strong subsidence and anticyclone associated with high SLP intensified over the SE Atlantic Ocean throughout the vertical layer (600–925 hPa) associated with the mid-latitude frontal system south of 40° S (< 30° W, < 10° E). Very weak zonal winds and very strong northward meridional winds developed on 20–21 August 2017 as the jet amplified and pushed northward. Boundary layer BC was low on 18-19 Aug. BLH was elevated over the 0-10° E, 15-25° S on 18, 19 Aug and south African coast on 21 Aug. due to the strong mid-latitude jet around 30° S.

23-28 Aug.	26, 28 Aug.	20° W–15° E, 5–25° S	26, 28 Aug.	Relatively slow-moving moisture advection corresponded to the weakening of the AEJ-S. Cut-off low in the west of the flight region (20° W-0, 20-30° S) with high SLP was built up south of 30° S, 10° W-20° E on 26 Aug. Mid-level/upper-level trough amplified, leading to southward winds over the SE Atlantic coastal region on 28 Aug.
29–31 Aug.	30, 31 Aug.	30° W–20° E, 5–25° S	x	Relatively fast-moving moisture advection along with the enhancement of the AEJ-S. Strong St. Helena High was observed over South Atlantic. BLH over the south Atlantic (20-30° S, 20° W-0°) was elevated north of the strong mid-latitude jet max at 40° S. The impact of the mid-latitude cyclone was small over the flight region due to its confined development over the south of 30° S.
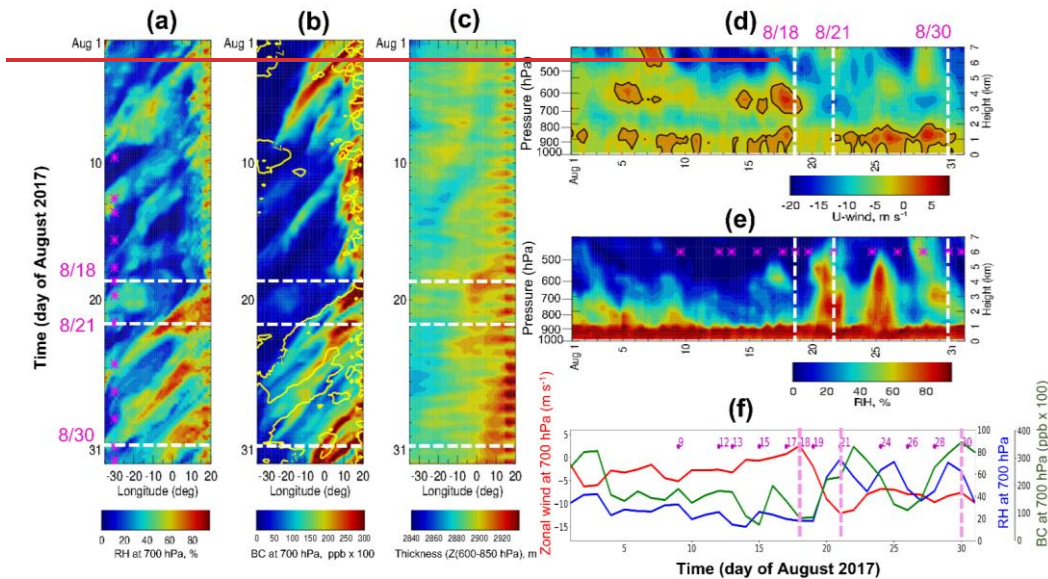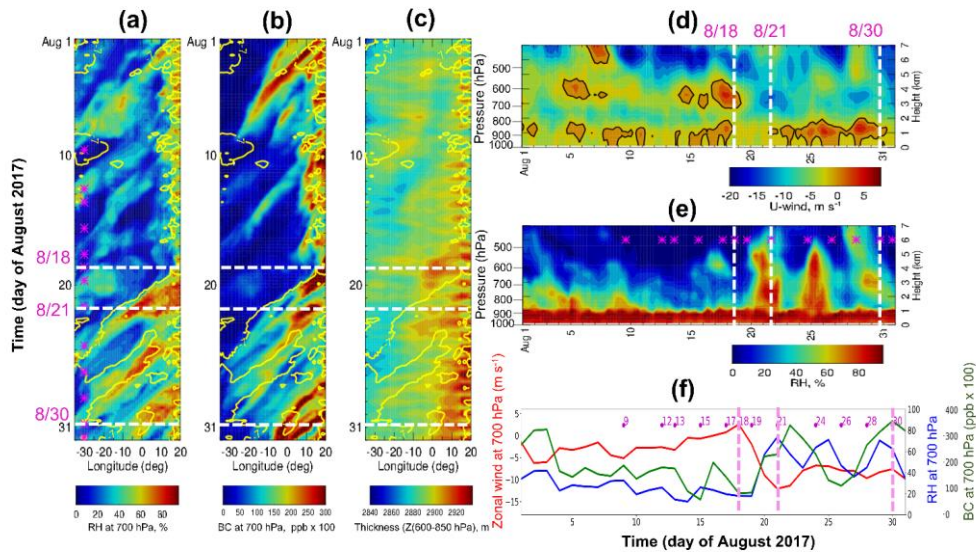
Figure 7. Longitude-time cross-section of 6-hourly (a) 700 hPa RH (%), (b) 700 hPa BC aerosol (shading, ppb x 100), and (c) thickness (geopotential height difference (600-850 hPa); high values (> 2920 m) over a South African plateau represents the heat low, m) averaged over 5–7° S during August 2017. (a-c) are overlaid by 700 hPa zonal wind isotach (yellow line, -7 m s⁻¹). <s>, (c) thickness (geopotential height difference (600-850 hPa); high values (> 2920 m) over a South African plateau represents the heat low, m) averaged over 5–7° S during August 2017.</s> (d–e) Altitude-time cross-section of zonal wind and RH at 6° S, averaged over 0–10° E during August 2017. The black contour in (d) represents the 0 value of zonal wind. (f) Daily time series of the 700 hPa zonal-wind (red line, m s⁻¹), 700 hPa RH (blue line, %), and 700 hPa BC (green line, ppb x 100) averaged over 5–7° S and 0–10° E. The dashed white <s>dashed</s> lines indicate the flight days investigated further in this study, and the magenta asterisks (and numbers in f) represent the flight days during the August 2017 deployment.

The strongest free-tropospheric winds occur approximately 3 degrees further north in August 2017 than in September 2016, or between 5-7° S (section 3.1). The Hovmöller diagram in Fig. 7 indicates relatively dry conditions until 18 August 2017, with weak easterlies over the Atlantic Ocean (Figs. 7(a, b)). The BC aerosol layer coincides with the lower altitude of the AEJ-S and RH (Fig. 7b). The heat low strengthens considerably as the month progresses (Fig. 7c). Strongly easterly winds, or the AEJ-S, do not become apparent until August 20 and their maximum height is lower (~ 700 hPa, ~3 km) in August than in September (Figs. (2, 5, 7d)). In August 2017, there is another easterly jet above 500 hPa, and this is unusually strong compared to the climatology (Ryoo et al., 2021; Fig. 7d). Relatively dry free tropospheric conditions (RH is < ~60 % (q ~ 8 g

kg^{-1})) over the ocean continue until 18 August 2017, and thereafter shift to a moist regime after 20 August 2017 when moist plumes develop (Figs. 7(e, f)), coinciding with the development of the AEJ-S over the continent. A similar feature is evident in the water vapor mixing ratio (Fig. S4).

395
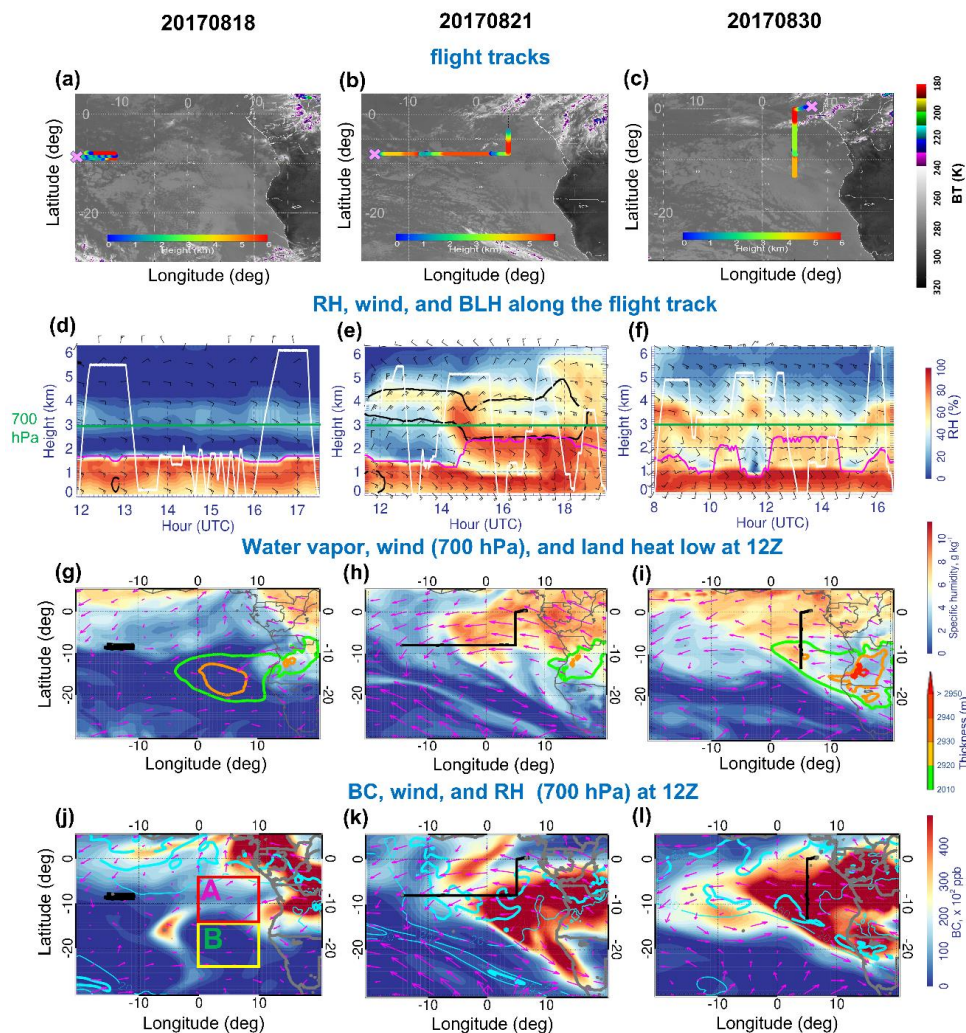
Figure 8. (a–c) The horizontal flight tracks during the August 2017 ORACLES deployment plotted on Meteosat IR 10.8 μm imagery at 13:45 UTC (shading is Brightness Temperature (BT), K). The color of the flight track represents the altitude of the P-3 flight along the horizontal flight track. (d–f) Curtain plot of RH along the P-3 flight track during 18, 21, and 30 August 2016. The white contour represents the flight profile. The magenta line in (d–f) represents the BLH along the flight track. Bold black contours in (d–f) are zonal winds (-8 m s⁻¹). The green line in (d – f) indicates the 700 hPa level. (g – i) Map of 700 hPa q (color shading, g kg⁻¹) and 700 hPa horizontal winds (vectors, m s⁻¹) overlaid by thickness (thickness: geopotential height (Z) difference between 600 hPa and 850 hPa, color line contour; high values (> 2920 m) over land represents the heat low) at 12:00 UTC on 18, 21, and 30 August 2017, respectively. (j–l) Map of 700 hPa BC (shading, ppb x 100) overlaid by 700 hPa RH (thick cyan line: 60, thin cyan line: 20, %) and 700 hPa horizontal winds (vectors, m s⁻¹) at 12:00 UTC 18, 21, and 30 August 2017. The black line in (g-l) represents the horizontal flight track on the given day. The magenta (yellow) box in Fig. 8j refers to region A; 0-10° E, 5-15° S (region B; 0-10° E, 15-25° S).

The flight tracks with their altitudes and RH superimposed for three August 2017 flights are shown in Fig. 8. The 18 August 2017 flight was coordinated with one from the CLARIFY (Haywood et al., 2021) campaign out of Ascension Island. The 21 August 2017 flight was a transit flight from Ascension back to São Tomé. The 30 August 2017 'routine' flight went along 5° E south to about 13° S and back. These flight days possess unique and interesting meteorological characteristics that help interpret the monthly evolution.

The remote atmosphere sampled on 18 August 2017 near Ascension Island was dry (RH < 40%) above ~5 kft (~–1.5 km), with the flight back to Sao Tome on 21 encountering an abrupt change to a moister free troposphere at ~ 7° W (Fig. 8e). This moisture tongue is tied to northeasterly wind advection from moist convection occurring mostly from north of 5–10° S (Figs. 8(b, e)). The north-south flight along 5° E on 30 August 2017 sampled more consistently moist conditions (Figs. 8(e, f)). Contrary to the relatively uniform BLH on 18 August 2017, (mainly due to the long duration of the flight over the same location), the BLH on 21 and 30 August 2017 varies, with alternatively dry (RH < 40%) and moist (RH > 60%) boundary layers. The AEJ-S on 21 and 30 August 2017 is strong, penetrating further west (Figs. 8(e, f)). The BC aerosol is also modulated by the intensity and horizontal extent of zonal wind (e.g., AEJ-S) around 700 hPa around 5-7° S, with some and transported by the recirculateding flow associated withback around the anticyclone toover the continents (Figs. 8(j-l)).
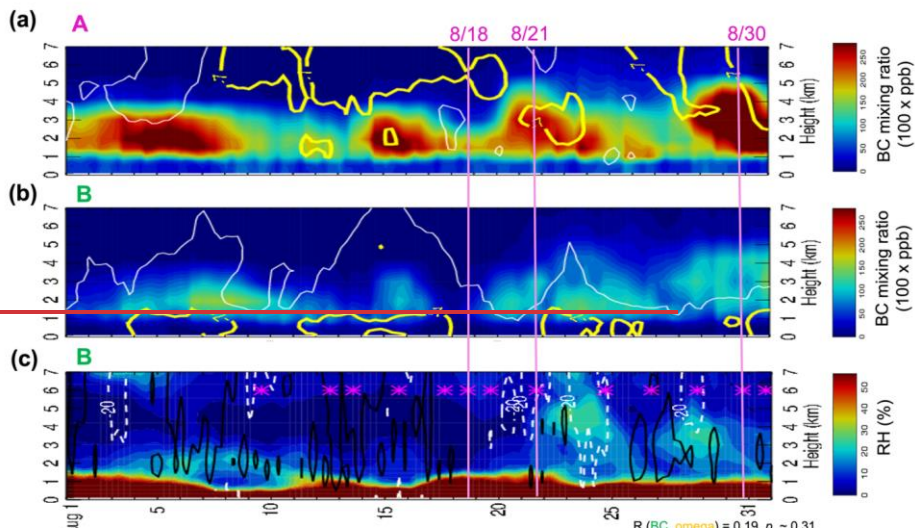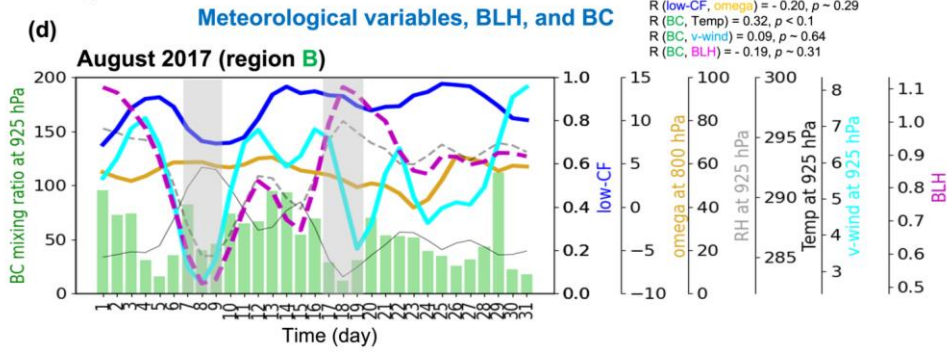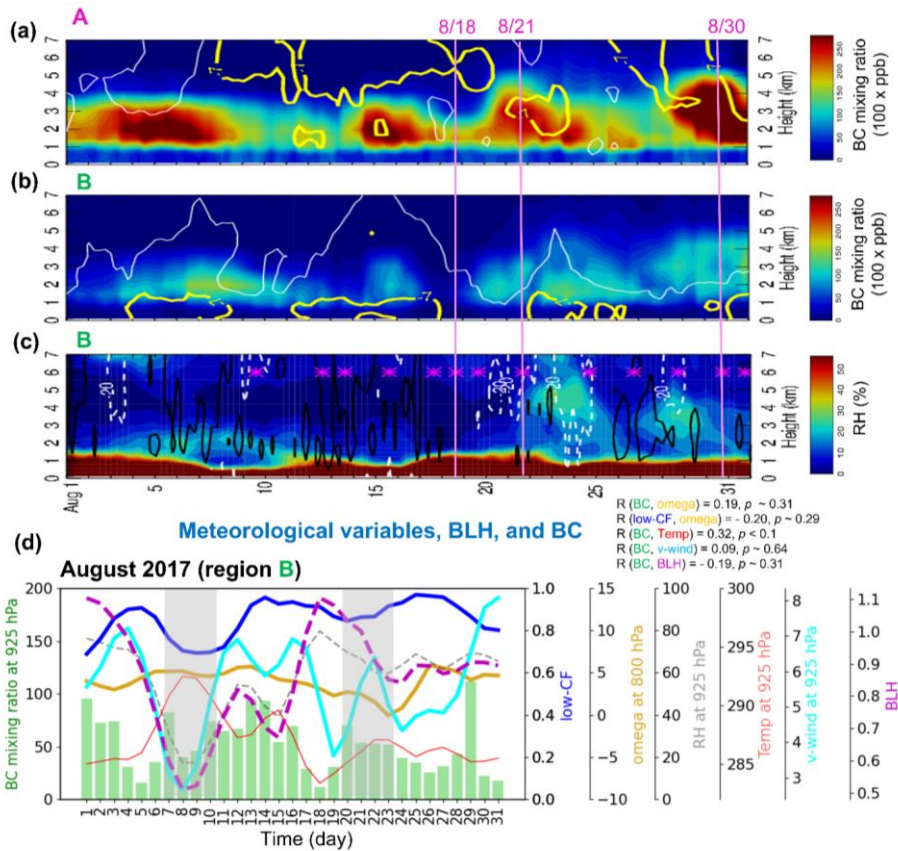
Figure 9. (a–b) Time-altitude cross section of 6-hourly BC (shading, ppb x 100) overlaid by 6-hourly zonal wind isotachs at -7 and 0 m s⁻¹ (thick -yellow and thin -white lines respectively) averaged over (a) region A (0–10° E, 5–15° S) and (b) region B (0–10° E, 15–25° S) in August 2017. (c) The same as (b) but for 6-hourly RH (shading, %) overlaid by 6-hourly vertical velocities of -20 and 50 hPa day⁻¹ (dashed white dashed and solid black solid lines respectively; positive values represent subsidence) averaged over region B. (d) Time series of daily-mean 925 hPa BC (green bar, ppb x 100), 800 hPa vertical velocity (omega, ω) (gold line, hPa day⁻¹), 925 hPa RH (gray dashed gray line, %), 925 hPa temperature (black solid red line, K), 925 hPa meridional wind (cyan solid cyan line, m s⁻¹), BLH (dashed magenta dashed line, km) and low-CF (blue line) over region B. Each color line represents the 3-day running

430 **mean. The asterisk in (c) represents the August 2017 flight days. The pink solid lines in (a-c) refer to the three flight days. The light gray shadings in (d) represent the two periods having different BC-RH conditions.**

Figure 9 illustrates that most of the BC is located between 2-3 km, increasing in altitude towards the end of August 2017. The BC altitude is generally lower than that in September (compare Figs 9a and 4a), consistent with a lower AEJ-S core in August

435 compared with September (Figs. 9(a, b). BC and RH in the mid-troposphere (~3-4 km) covary over region B after 20 August 2017. Interestingly, the moisture can extend higher in altitude than the BC within the ERA5/CAMS reanalysis. Boundary layer BC aerosols are slightly more abundant in August 2017 compared to September 2016 (Figs. (4d, 9d)); the "smoky" boundary layer is well observed near Ascension Island in August 2017 (Zhang and Zuidema, 2019; Pennypacker et al., 2020). The boundary layer BC mixing ratio is higher over region A than B (Figs. (8h, 9(a, b)).

440 Clear relationships exist between low-CF and the boundary BC – temperature – RH for a few cases (e.g., 7-9 August 2017 and 17-19 August 2017), but in general, there is no clear statistically-significant correlation. AEJ-S is also less associated with LLJ in August (Fig. S5). Mean subsidence in August 2017 is slightly weaker than in September 2016 and the correlation between subsidence and low-CF is insignificant at the daily time scale (Fig. 9d), consistent with De Szoeke et al. (2016) and Adebiyi and Zuidema (2018).

445
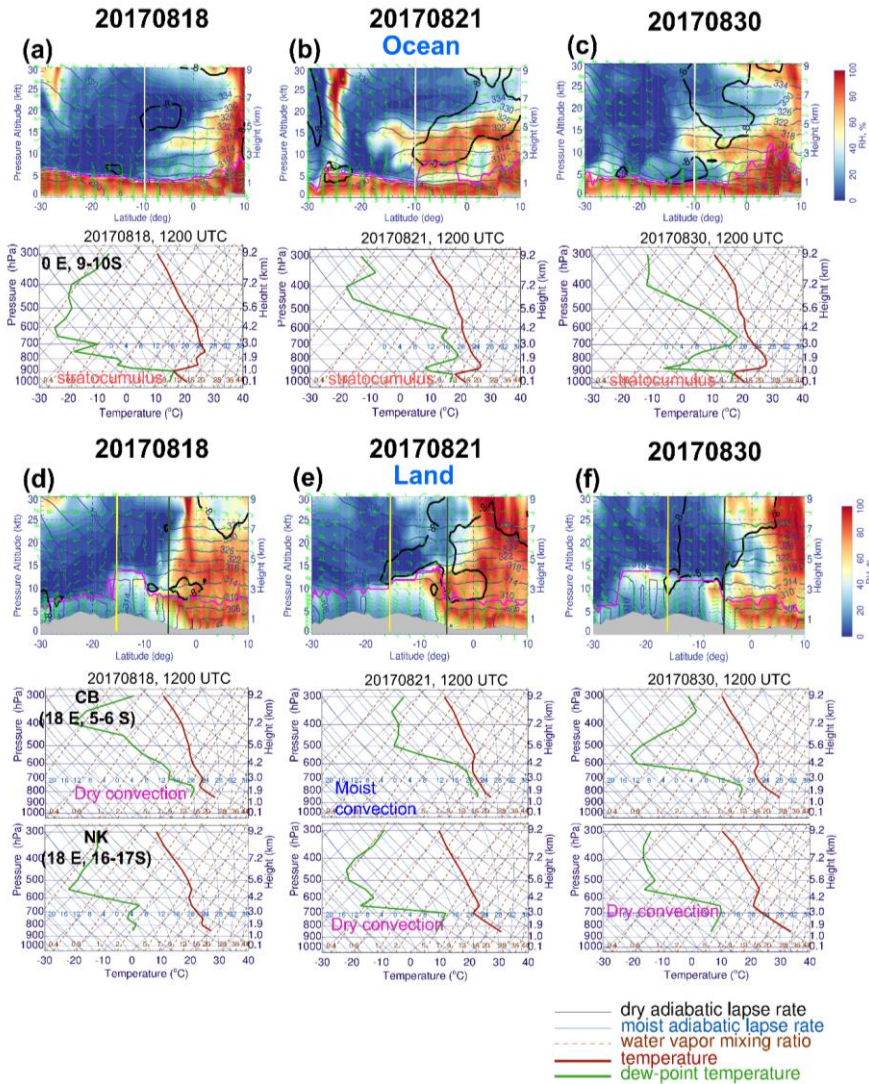
Figure 10. (a–c) *Ocean*: latitudinal cross-section of RH (shading, %), horizontal winds (wind barbs, green, m s^{-1}), θ (navy, K), and BLH (magenta, m) at 0° E (top) and Skew-T log-P diagram averaged over 0° E and 9–10° S (bottom: from the left) at 12:00 UTC

450 18, 21, and 30 August 2017. Bold black contours are zonal wind (-8 m s^{-1}). (d–f) *Land*: the same as in (a–c) except for the cross-section at 18° E and Skew-T log-P diagram averaged over 18° E and 5–6° S (CB: Congo basin) and 18° E and 16–17° S (NK: Namibian-Kalahari dryland). The gray-filled area represents the topography. The vertical lines in the cross-section plots refer to the latitude we examine.

Fig. 10 communicates the vertical structure of the moisture during the three flights highlighted in Fig. 8. High humidity levels (RH> 60 %) remain confined over the continents on August 18, 2017 (Fig. 10a). After 18 August 2017, moisture began to advect off of the continent at 700 hPa (Fig. 10b). Both moist and dry convection over land were more effective at moistening the mid-levels (700–600 hPa) on 21 and 30 August 2017, after the AEJ-S became active, than on 18 August 2017.

The cross-sections show that the horizontal temperature gradient over land is weak, as expected for the Tropics (Fig. 10a). Note that the moisture at all levels does not extend as far south as in September. Over the land, the temperature inversion layer sits above the unsaturated, dry layer over the land, and dew point temperature follows a constant water vapor mixing ratio (21, 30 August in the bottom panels of Figs. 10(e, f)), confirming that dry convection occurs after 20 August 2017. Considering conditions were uniformly dry before 20 August, neither dry nor moist convection was likely to be initiated in August 2017 over the Kalahari dryland (NK: 18° E, 16–17° S). Here the surface temperature increases consistently from 18 August to 30 August, and the dry convective layer deepens (Figs. 10(d-f)). This transports more moisture upward, south of 10° S, into the 850–600 hPa altitude range. Over the Congo basin (CB: 18° E, 5–6° S), the depth of the relatively moist near-surface layer is highest on 21 August and highly variable between the three soundings. Unlike September 2016, CAPE is generally low. This is consistent with the lower rainfall in that month as compared to September. Note that we see an increase in surface dewpoints from August 18 to August 21 over land, which can help increase the RH in dry convection regions at 700 hPa and along the flight track in August 2017.

470
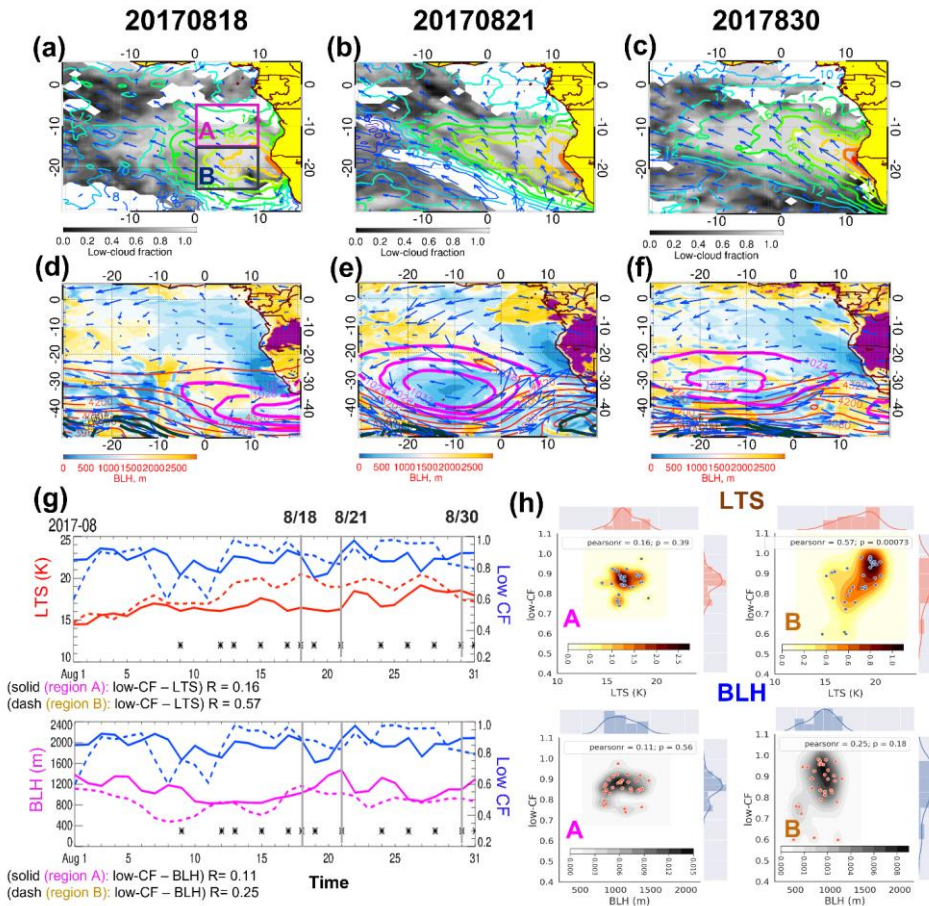
Figure 11. Map of (a–c) daily mean low-CF (shading) overlaid by LTS (contour, K) and 925 hPa horizontal winds (vectors, m s⁻¹),
(d–f) BLH (shading, m) overlaid by 600 hPa horizontal winds (vectors, m s⁻¹), 600 hPa geopotential height (red lines, m), and sea
level pressure (SLP; dark green (low-pressure: 996, 1000, 1004), and magenta (high-pressure: 1024, 1028, 1032) lines, hPa) at 12:00
UTC 18, 21, and 30 August 2017. (g) (Top) time series of daily mean low-CF (blue lines) and daily mean LTS (red lines, K), and
(bottom) daily mean low-CF (blue lines) and daily mean BLH (magenta lines, m) averaged over region A (0–10° E, 5–15° S; solid
lines) and region B (0–10° E, 15–25° S; dashed lines) during August 2017. All flight days (18, 21, and 30 August 2017) are marked

by an asterisk (gray vertical lines). The purple shading over land in (d–f) refers to BLH higher than 3250 m. (h) The 2-D joint pdf (shading) with scatter plot are shown with 1-D histogram (pdf in line) of (top) daily mean low-CF and LTS and (bottom) daily mean low-CF and BLH over region A (left) and B (right) during August 2017. The solid line in (a) indicates region A (magenta box) and region B (navy box), respectively. The pearsonr in (h) refers to Pearson's correlation coefficient with its statistical significance (*p-value*).

During August 2017, low-CF is also positively correlated with LTS, strongest in region B, with a similar correlation coefficient as September 2016 (R~ 0.57, top panel of Fig. 11g). The BLH tends to be higher over the open ocean (10–40° W, 10–40° S) and land than near the west coast of Africa (Figs. 11(d–f)). The mid-latitude jets are very strong, but remain mostly confined south of 30° S. The mid-latitude frontal system nevertheless influences the local circulation, enhancing SE Atlantic anticyclones on the west and cyclones on the east of a mid-level trough leading to cloud clearing on 18 August 2017 (Fig. 11 (a, d)) and 21 August 2017 (Figs. 11 (b, e)). The ~~high~~ increased low-CF is weakly associated with the low BLH (e.g., 22 August 2017 in Fig. 11g) and low-CF is almost larger than 0.8, rendering poor correlations to meteorological variations. The distributions of LTS, BLH, and low-CF differ over regions A and B (Fig. 11h), particularly with tight relation between LTS and low-CF over region B.

The LTS is generally lower in August than in September over both regions, implying that the atmosphere is less stable in August, with LTS increasing as the month progresses. The decreased atmospheric stability may reflect the influence of the mid-latitude frontal system, especially in region B where recurrent cloud clearing by local pressure and wind ~~change~~ patterns associated with the intensified mid-latitude frontal systems. The mid-level flow and SLP patterns for all August 2017 flight days are provided in Fig. S14.

3.3 Deployment year 3 (São Tomè, October 2018)

The final deployment of ORACLES also occurred in São Tomé (0.34° N, 6.73° E), in October 2018. The equatorial deep convective band moves south in October (Adebiyi et al., 2015), and biomass burning is substantially less (Redemann et al., 2021; Zhang and Zuidema, 2021). Thus, despite a pronounced Kalahari heat low supporting strong free-tropospheric easterlies to its north, less BC is ultimately advected westwards. Continental convective systems migrate southward from 5° S, and mid-latitude frontal systems also assist the transition to austral summer. The AEJ-S was slightly weaker compared to the climatological mean, as were the LLJ and the southern Atlantic anticyclone (Ryoo et al., 2021), especially as the month progressed; the strength of the AEJ-S and heat low over land exceeded September values from early to mid-October, but weakened by late October 2018 (Fig. 12, Figs. S11-S12). The monthly mean low-CF is not much lower than the climatological mean, despite a warmer-than-climatology SST. The low-CF is the largest of all deployment months, with more mid-tropospheric moisture potentially reducing ~~perhaps~~ entrainment drying from above (Zhang and Zuidema, 2021). The

510 characteristics of synoptic-scale and convective features during the flight days in October 2018 deployment are summarized in Table 3.

Table 3. Characteristics of synoptic-scale features over SE Atlantic during the October 2018 deployment. The P-3 flights were available in October 2018. MFS represents the mid-latitude frontal system affecting the flight region on that day (x represents no effect).

Dates	Flight days	Lon/Lat domain	MFS	Synoptic description
1–5 Oct.	2, 3, 5 Oct.	20° W–20° E, 0–25° S	x	Fast-moving (~12.8 m s^{-1}) convection mostly from developing continental convection (< 5° N) marching westward along with the strong AEJ-S. Strong westerly passing by. Extensive high SLP developed over the South Atlantic (30° W-20° E, 25-45° S). The impact of the mid-latitude frontal system on the flight regions was minimal due to its confined development further south of 40° S, 30° W-0.
6–10 Oct.	7, 10 Oct.	20° W–20° E, 0–25° S	7, 10	Moderate convection development. The strong AEJ-S persisted. Strong southward wind near the coast as westerly weakened on 10 Oct. Developing mid-latitude frontal system was observed 20° W-0, south of 30° S. BLH over the SE Atlantic was notably low on 7 Oct.
11–12 Oct.	12 Oct.	20° W–20° E, 5–25° S	x	A weakening of the AEJ-S, weak moisture advection from the African continent. The impact of the mid-latitude cyclone on the flight region during this period was small due to its confined development over the south of 30° S.
14–22 Oct.	15, 17, 19, 21 Oct.	30° W–15° E, 5–25° S	15, 17, 21	Slowly propagating (~6.4 m s^{-1}) moisture transport from land to the ocean. Further moisture transport as the AEJ-S strengthened. Subsidence and large-scale anticyclone were enhanced over the SE Atlantic Ocean. Mid-latitude and upper-level flows were tied to the intensification of the surface low over the southwest of the flight region (20° W-0, 25-50° S) on 15 and 21 Oct.
22 –28 Oct.	23, 25 Oct.	20° W–20° E, 5–25° S	23	Continental convection marched further south (< 20° S) over land. Cooling down of temperature and a weakening of both latitudinal moisture and temperature gradient over land. A weakening of the AEJ-S. BLH over land on 23 Oct. was noticeably lower compared to other flight days.
28–31 Oct.		20° W–20° E, 5–25° S	30	Moisture transport from land to ocean, along with the restrengthening of the AEJ-S. Anticyclone associated with the high SLP and the west of the ridge of the mid-latitude mid- and upper-level trough facilitated the northward flow over the coast of southern Africa.

515
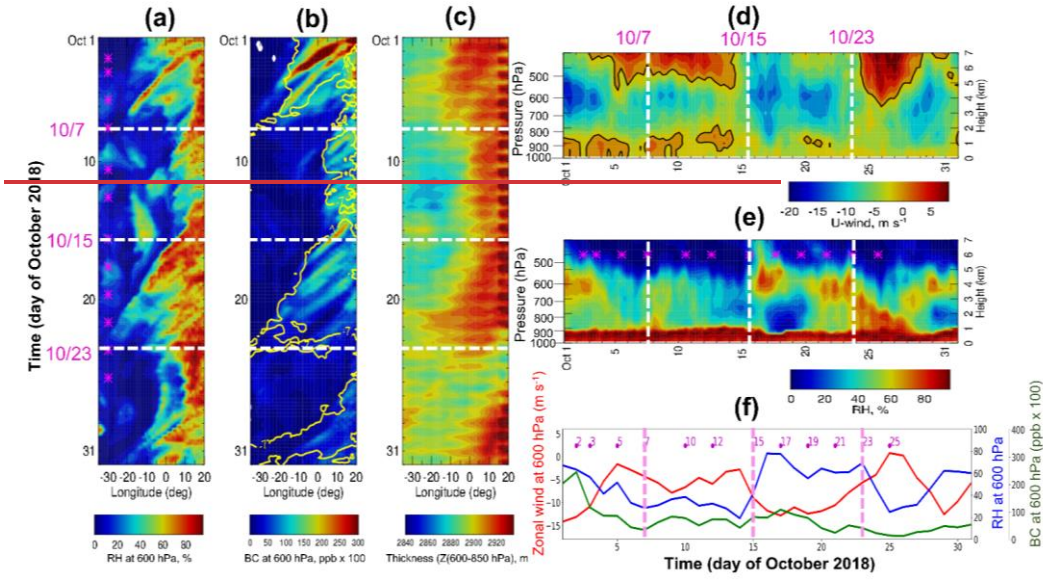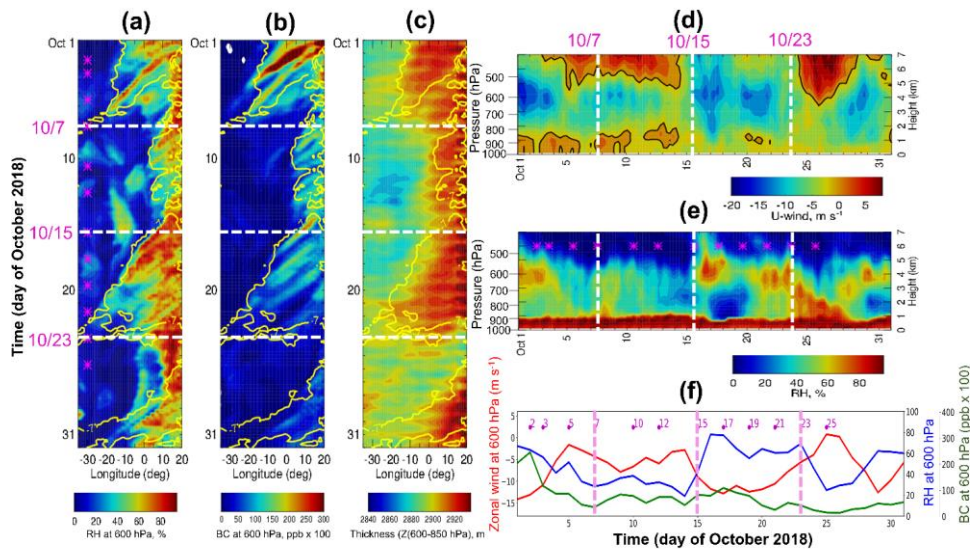
Figure 12. Longitude-time cross-section of 6-hourly (a) 600 hPa RH (%), (b) 600 hPa BC aerosol (shading, ppb x 100)~~, and (c) thickness (geopotential height difference (600-850 hPa); high values over a South African plateau represents the heat low, m) averaged over 8-10° S during October 2018.~~ (a-c) are overlaid by 600 hPa zonal wind isotach (yellow line, -7 m s⁻¹). ~~, (c) thickness (geopotential height difference (600-850 hPa); high values over a South African plateau represents the heat low, m) averaged over 8-10° S during October 2018.~~ (d–e) Altitude-time cross-section of zonal wind and RH at 10° S, averaged over 0–10° E during October 2018. The black contour in (d) represents the 0 value. (f) Daily time series of the 600 hPa zonal-wind (red line, m s⁻¹), 600 hPa RH (blue line, %), 600 hPa BC (green line, ppb x 100) averaged over 8–10° S and 0–10° E. The ~~white~~ dashed white lines indicate the flight days investigated further in this study, and the magenta asterisks (and numbers in f) represent the flight days during October 2018 deployment.

Figure 12 shows the 6-hourly time series as a function of longitude averaged over the 8-10° S latitude band (i.e., Hovmöller diagram) of RH, BC, and zonal wind at 600 hPa and heat low during October 2018. BC is also well modulated by AEJ-S, but its magnitude decreases significantly by the end of October when the biomass burning season tapers off amidst increasing RH indicative of southward-moving convection (Figs. 12(a, b)). After the easterlies weaken, the BC aerosol outflow reduces (e.g., 7-14 October, and after 26 October; Figs. 12(a, b, f)). The modulation of the AEJ-S by the heat low is clear, similar to the other deployments (Figs. (2, 7)). The AEJ-S leads to high RH by 1–2 days, indicating that AEJ-S can transport elevated moisture from land to the ocean (Fig. 12f; Fig. S6).

This flow changes dramatically as the month progresses, however. From 1–22 October 2018, high RH is propagated over
535   the ocean by a strong AEJ-S. By 23–28 October 2018, RH remains high over the continent, but does not propagate westward,
because the mid-tropospheric winds are weak (Figs. 12(e, f)). The low-level easterly winds are also weak (Fig. 12d).
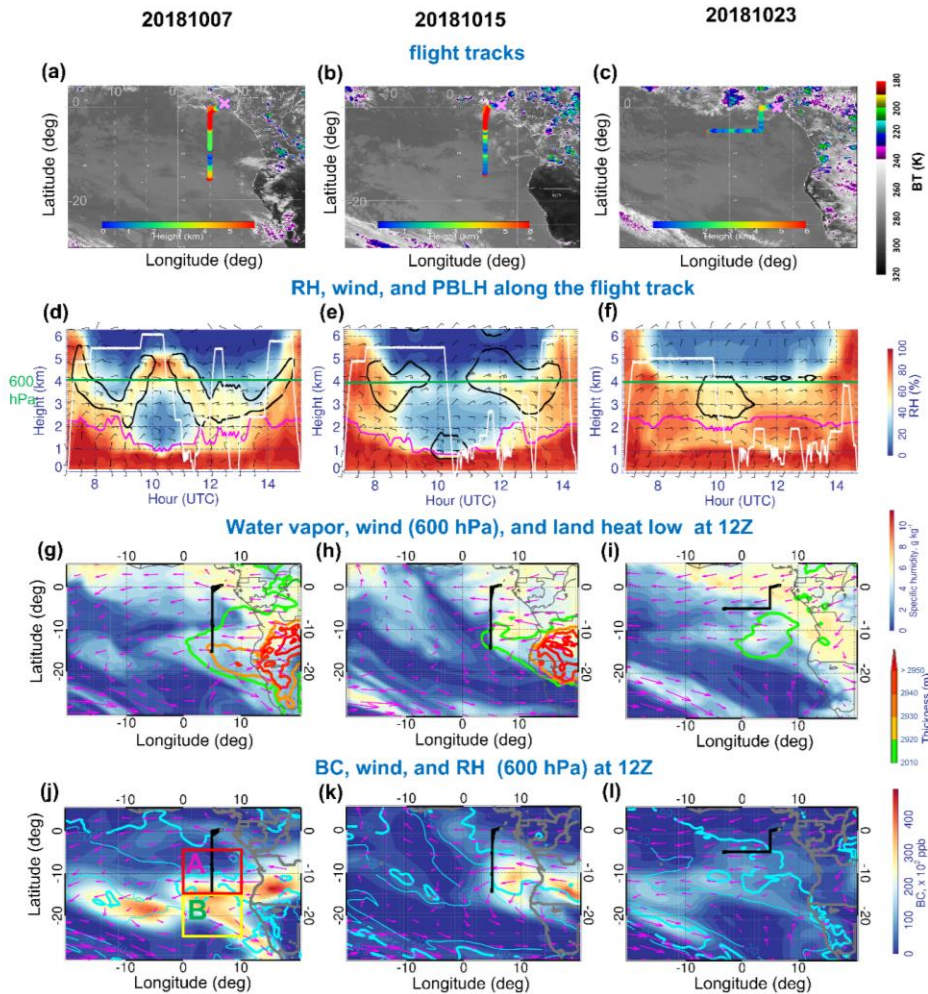
Figure 13. (a–c) The horizontal flight tracks during October 2018 ORACLES deployment plotted on Meteosat IR 10.8 µm imagery at 13:45 UTC (shading is Brightness Temperature (BT), K). The color of the flight track represents the altitude of the flight along the horizontal flight track. (d–f) Curtain plot of RH along the flight track during 7, 15, and 23 October 2018. The white contour represents the flight profile. The magenta line in (d–f) represents the BLH along the P-3 flight track. Bold black contours in (d–f) are zonal wind (-8 m s^{-1}). The green line in (d–f) indicates the 600 hPa level. (g – i) Map of 600 hPa q (color shading, g kg^{-1}) and 600 hPa horizontal winds (vectors, m s^{-1}) overlaid by heat low (thickness: geopotential height (Z) difference between 600 hPa and 850 hPa, color line contour; high values (> 2920 m) over land represents the heat low) at 12:00 UTC on 7, 15, and 23 October 2018, respectively. (j–l) Map of 600 hPa BC (shading, ppb x 100) overlaid by 600 hPa RH (thick cyan line: 60, thin cyan line: 20, %) and 600 hPa horizontal winds (vectors, m s^{-1}) at 12:00 UTC 7, 15, and 23 October 2018. The black line in (g-l) represents the horizontal flight track on the given day. The magenta (yellow) box in Fig. 13j refers to region A; 0-10° E, 5-15° S (region B; 0-10° E, 15-25° S).

Satellite imagery further indicates that substantial deep convection (brightness temperatures < 230 K) develops over the continent north of 10° S, starting mid-October 2018, spreading southward to northern Namibia and Botswana by 23 October 2018 (Figs. 13(a, c)). Routine flights along 5° E occurred on 7 October 2018 to 15° S, and on 15 October 2018 to 14° S, with the 23 October 2018 survey flight going west along 5° S. Like the other deployment months, we chose three October flight cases based on their unique meteorological and aerosol features. RH exceeded 60% for all three flights (Fig. 13f). Between 7 to 15 October 2018 (around 9:00 – 11:00 UTC shown in Figs. 13(d, e)), a strong mid-level AEJ-S also advected moisture (RH > 60%), leading to moist (RH > 60%) conditions at ~ 15 kft, (or ~ 4.5 km). Moist air is sampled along the flight track on 23 October 2018, along with an elevated marine BLH (Figs. 13(c, f)). The core latitude of the AEJ-S varies day by day.

The AEJ-S is strong on 7 and 15 October 2018 but weakens considerably around 10°S on 23 October 2018 (Fig. 13f). This could be tied to the collapse of the dome of warm, dry air over the southern African highlands and a breakdown of the 600 hPa anticyclone over southern Africa (Fig.13i). This also led to weaker moisture transport to the ocean at the south of 10° S on 23 October 2018. Two possible causes are: 1) the mid-latitude waves associated with a strong upper-level disturbance influence the breakdown of the dome of hot dry air (Kuete et al., 2021), and 2) convection reduces the temperature gradient by increasing high cloud cover over the region, limiting surface heating over the Kalahari-Namib dryland. (Figs. 13c). The heat low reforms toward the end of the month (Figs. 13(g-i)). Different BC aerosol transport patterns are also observed in flight days in October 2018. The intensity of the horizontal transport of BC largely aligns with the strength of the AEJ-S) and the recirculating flow (Figs. 13(j-l)). The extensive BC transport over the ocean is much more suppressed on 15 and 23 October than on 7 October 2018.
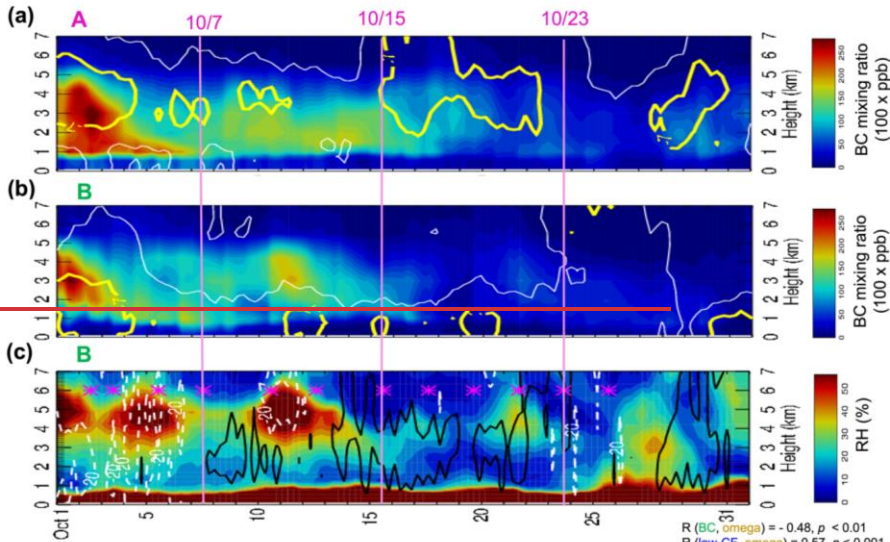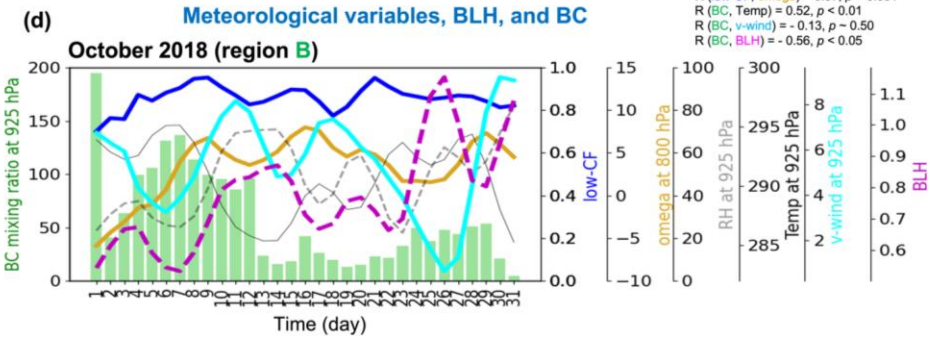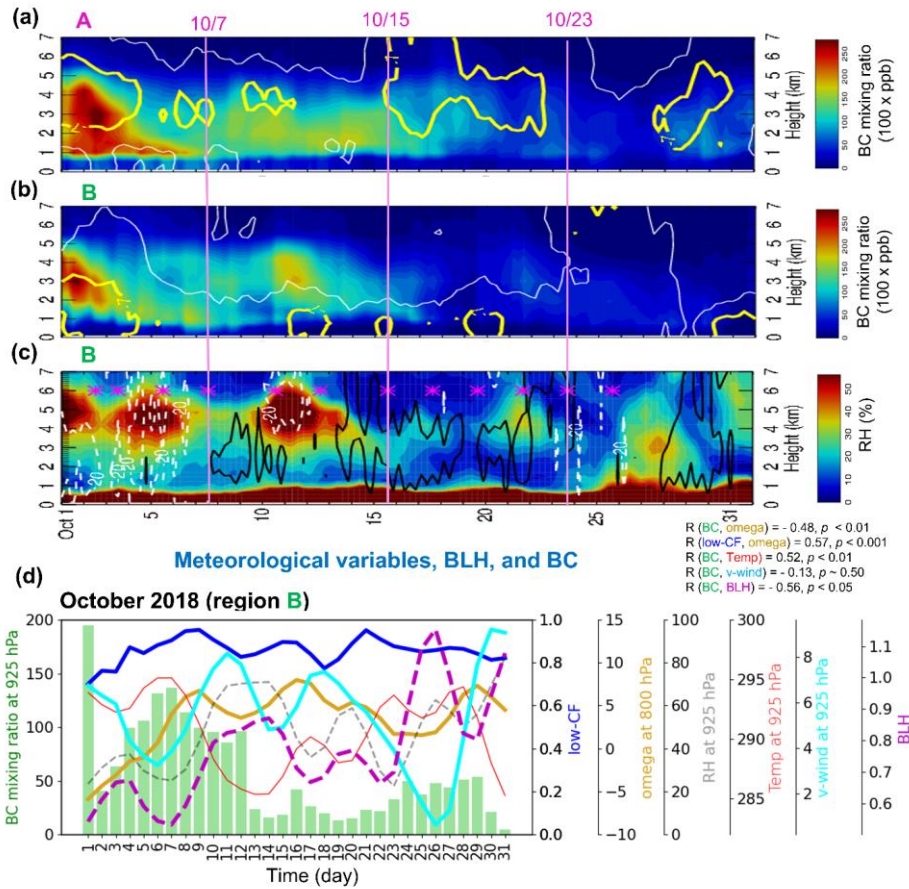
Figure 14. (a-b) Time-altitude cross section of 6-hourly BC (shading, ppb x 100) overlaid by 6-hourly zonal wind isotachs at -7 and 0 m s^{-1} (thick -yellow and thin -white lines respectively) averaged over (a) region A (0–10° E, 5–15° S) and (b) region B (0–10° E, 15–25° S) in October 2018. (c) The same as (b) but for 6-hourly RH (shading, %) overlaid by 6-hourly vertical velocities of -20 and 50 hPa day^{-1} (dashed white dashed-and solid black solid-lines respectively; positive values represent subsidence) averaged over region B. (d) Time series of daily-mean 925 hPa BC (green bar, ppb x 100), 800 hPa vertical velocity (omega, ω) (gold line, hPa day^{-1}), 925 hPa RH (dashed gray dashed-line, %), 925hPa temperature (black-solid red line, K), 925 hPa meridional wind (solid cyan line-solid,

m s⁻¹), BLH (dashed magenta ~~dashed~~ line, km), and low-CF (blue line) over region B. Each color line represents 3-day running mean.
The asterisk in (c) represents the October 2018 flight days. The pink solid lines in (a-c) refer to the three flight days.

Figure 14 illustrates the time evolution of coupled BC aerosol–meteorological variables and how they relate to low-CF in October 2018. The covariation between BC–RH in the mid-troposphere (3–4 km) is also observed in October 2018, with the RH increase extending higher in altitude than the BC. The aerosol loading decreases around mid-October 2018 while moisture variations continue; this was clearly shown when a frontal system passed by. An increased BC aerosol loading at 925 hPa correlates with an increased 925 hPa temperature up to 7 October (Fig. 14d). The subsidence – low-CF relationship in October 2018 is somewhat different from that in September 2016 and August 2017, in that subsidence and low-CF are positively correlated.
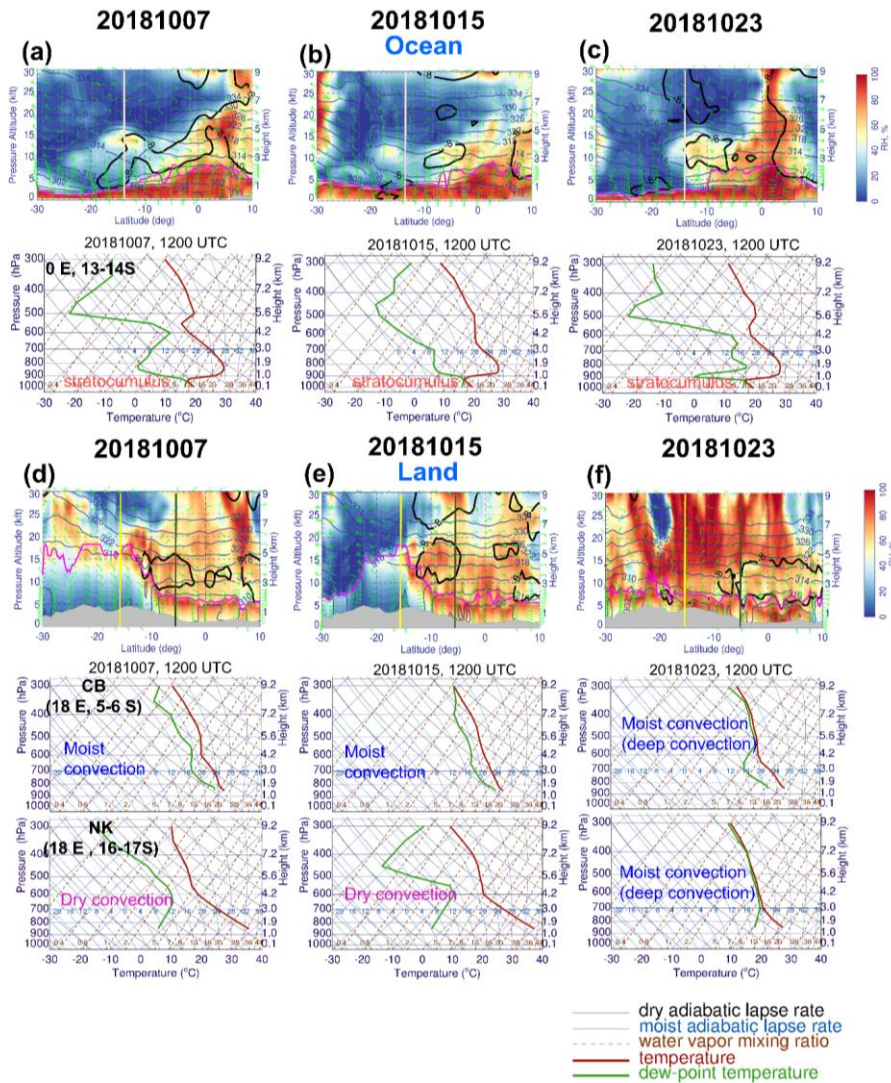
Figure 15. (a–c) *Ocean*: **latitudinal cross-section of RH (shading, %), horizontal winds (wind barbs, green, m s⁻¹), potential temperature (θ) (navy, K), and BLH (magenta, m) at 0° E (top) and Skew-T log-P diagram averaged over 0° E and 13–14° S (bottom:**

from the left) at 12:00 UTC 7, 15, and 23 October 2018. Bold black contours are zonal wind (-8 m s^{-1}). (d–f) *Land*: the same as in (a–c) except for the cross-section at 18° E and Skew-T log-P diagram averaged over 18° E and 5–6° S (CB: Congo basin) and 18° E and 16–17° S (NK: Namibian-Kalahari dryland). The gray-filled area represents the topography. The vertical lines in the cross-section plots refer to the latitude we examine.

Latitudinal cross-sections of moisture and winds along with soundings from three representative flight days indicate that the transport of moist plumes to the ocean is also a component of the AEJ-S in October (Figs. 15 (a–c)). A noteworthy feature of the 7 October sounding over the ocean is its resemblance to the "dry convection" layer over land, indicating that this moist plume also likely originated from dry convection over the land and was then advected westward by the AEJ-S (Figs. (5c, 15a)). On 7 and 15 October, dry convection was still dominant over the Namibia-Kalahari dryland (18° E, 16–17° S) while moist convection developed over the Congo basin (18° E, 5–6° S). Later, as dew point temperature no longer followed the constant water vapor mixing ratio line over the dryland and approached the temperature, indicating the dry convection transitioned to deep moist convection (top panel of soundings in Figs. 15(d–f)). On 23 October, the moist plumes with high RH (> 60%) reached 10–20° S (Figs. 15(d–f)) with moist convection over both Congo basins and Namibia-Kalahari dryland (see satellite image, Fig. 13c). Deep cloud layers, identified by locations where the dew point temperature matches the environmental temperature curves, are clearly shown on 23 October 2018 (soundings in both CB and NK in Fig. 15f). With such deep clouds, RH reaches ~ 100 %, indicative of heavy rainfall.
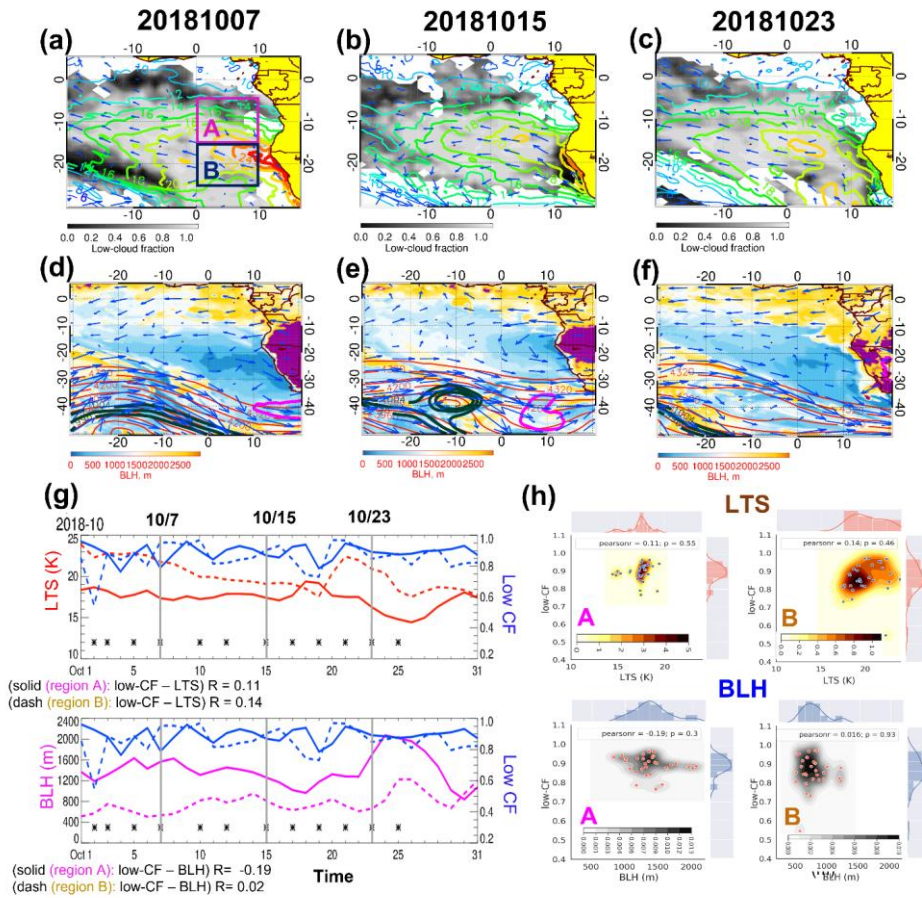
Figure 16. Map of (a–c) daily mean low-CF (shading) overlaid by LTS (contour, K) and 925 hPa horizontal winds (vectors, m s^{-1}), (d–f) BLH (shading, m) overlaid by 600 hPa horizontal winds (vectors, m s^{-1}), 600 hPa geopotential height (red lines, m), and sea level pressure (SLP; dark green (low-pressure: 996, 1000, 1004), and magenta (high-pressure: 1024, 1028, 1032) lines, hPa) at 12:00 UTC 7, 15, and 23 October 2018. (g) (Top) time series of daily mean low-CF (blue lines) and daily mean LTS (red lines, K), and (bottom) daily mean low-CF (blue lines) and daily mean BLH (magenta lines, m) averaged over region A (0–10° E, 5–15° S; solid

lines) and region B (0–10° E, 15–25° S; dashed lines) during October 2018. All flight days (7, 15, and 23 October 2018) are marked
by asterisk (gray vertical lines). The purple shading over the land in (d–f) refers to BLH higher than 3250 m. (h) The 2-D joint pdf
(shading) with scatter plot are shown with 1-D histogram (pdf in line) of (top) low-CF and LTS and (bottom) daily mean low-CF
and BLH over region A (left) and B (right) during October 2018. The solid line in (a) indicates region A (magenta box) and region
B (navy box), respectively. The pearsonr in (h) refers to Pearson's correlation coefficient with its statistical significance (*p-value*).

The positive correlation between LTS and low-CF is weaker in October 2018 (e.g., 10° W–0, 5–15° S) and statistically more insignificant than during the other two deployment months (see Fig. 16), partially because neither the LTS nor low-CF vary much in October 2018, particularly over the north of 20° S. When the subsidence weakens compared to August and September, low-CF and LTS remain mildly correlated, especially at intermediate LTS values (16 – 20 K) (Fig. 16h, Zhang et al., 2009). Similar to August and September, the LTS–low–CF correlation in October is more evident in region B than in region A (Figs. 6g, 11g). As LTS strengthens, the low–CF increases, as shown in Figs. 16(a–c). The BLH is higher over the ocean (10–40° W, 10–40° S) and shallower near the west coast of Africa (Figs. 16(d–f)). Low-CF variability is also relatively invariant with BC aerosol (this is also clear in region A (0-10° E, 5-15° S)) while a stronger LLJ tends to reduce low-CF during October (Fig. S8(c)). The mid-tropospheric winds and LLJ, both strong during October 2018, are also the most correlated (R ~ 0.55, p-value < 0.01) of the three deployment months (see the AEJ-S - LLJ correlation analysis in Fig. S7). A sufficiently strong temperature inversion, moist and warm conditions associated with the mid-latitude frontal system may provide favorable conditions for both the AEJ-S and LLJ to develop together (Figs. 16(a-f)).

In particular, low-CF slightly decreased on 23 October 2018 (Figs. 16(c, g)), but the high cloud cover increased (not shown), indicating not only day-to-day variability but also that a cloud regime "transition" to deep convection (Fig. 15f) may occur, especially south of the flight region (< 20° S). The low clouds also tend to respond to the change in the BLH; large low-CF is weakly associated with a lower BLH on some days (e.g., 6, 18, 25, and 30 October 2018; the bottom plot in Fig. 16g), but the overall correlation between the BLH and low-CF is low and statistically insignificant (Fig. 16g). This can be partially explained by large day-to-day variability from passing mid-latitude frontal systems. The developing mid-latitude frontal systems, indicated by 1) the reduced St. Helena High and LTS, 2) decreasing SLP slightly east of the mid-level trough, and 3) misalignment of mid-level wind vector and mid-level geopotential height, promotes increased disturbance and vertical motion, eventually intensifying the frontal system (Holton, 2004). The mid-latitude upper-level disturbance also contributes to modulating the temperature gradient over SE Atlantic (Ryoo et al., 2021), ultimately affecting local circulation. Further examination of the mid-level flow and SLP patterns for all October flight days is shown in Fig. S15.
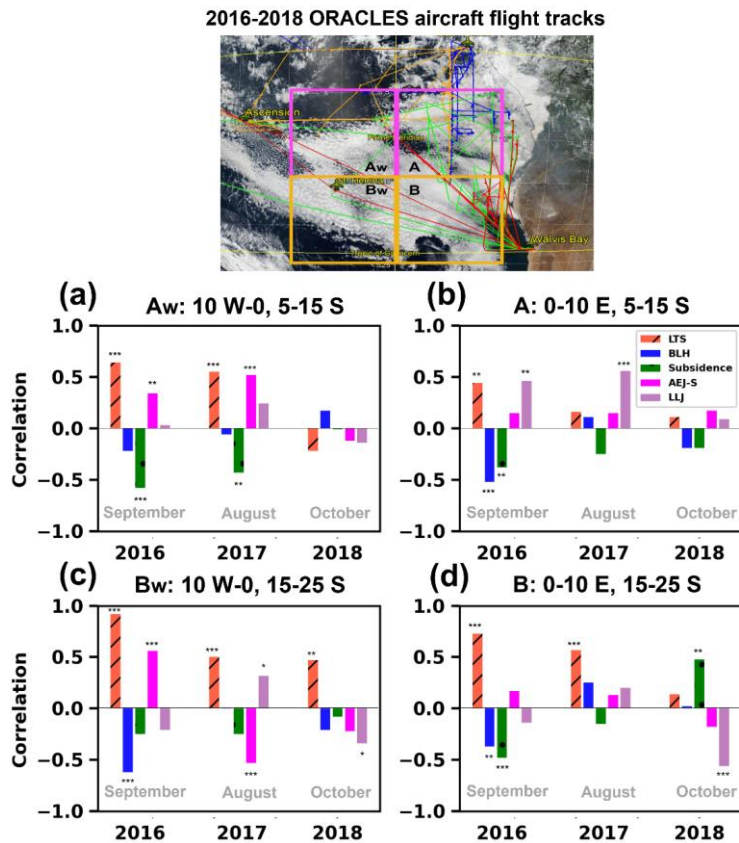
Figure 17. Bar plots of the linear correlation between daily mean low-CF and daily mean of the meteorological variables (LTS, BLH,
subsidence, AEJ-S, and LLJ) averaged over four subregions in the ORACLES flight regions over the SE Atlantic Ocean ((a) Aw:
10° W–0, 5–15° S, (b) A: 0–10° E, 5–15° S, (c) Bw: 10° W–0, 15–25° S, and (d) B: 0–10° E, 15–25° S) during the deployment months
(marked in the boxed regions over the top image with flight tracks). A and B correspond to the regions A and B shown in the previous
figures (e.g., Figs. 3, 4, 6; Figs. 8, 9, 11; Figs. 13, 14, 16), while Aw and Bw correspond to the west of the regions A and B, respectively.
*** (**, *) denotes when the correlation is statistically significant within 99% (95, 90 %) confidence interval (*p-value* < 0.01 (<0.05,
< 0.1)). The top panel represents the ER-2 flight tracks in 2016 (green), and the P-3 flight tracks in 2016, 2017, and 2018 (red, orange,
and blue, respectively). The top panel with flight tracks on a MODIS image and © Google Maps on 13 September 2018 is adapted
from Redemann et al. (2021).

4. Relationships between low cloud cover and meteorological variables

The linear relationship of meteorological variables to low-CF over SE Atlantic regions during each deployment month at a daily time scale is shown in Fig. 17. Daily mean Low-CF is positively associated with LTS for all deployment months except for north of 15° S (10° W–0, 15–5° S, Fig. 17c) in October. The LTS – low-CF relationship is weakest north of 15° S near the coast (0-10° E), in the vicinity of AEJ-S, moisture, and BC aerosols (Fig. 17b). BLH is also negatively associated with low-CF, especially in September. The relationships to low-CF are most pronounced in September for all subregions, with more variability in August and October. Subsidence is typically negatively correlated with low-CF, except for south of 15° S near the coast in October (Fig. 17d) at a daily time scale. Both AEJ-S and LLJ are positively correlated to low-CF in September and August north of 15° S but are negatively correlated in October (Fig. 17d). The AEJ-S and any aerosol will affect the subsidence, and this may be reflected in the jets (AEJ-S, LLJ)–subsidence relationship to low-CF. Also note this is reversed both north and south of 15° S near the coast (0–10° E, Figs. 17(b, d)), consistent with Andersen et al. (2020) except for September south of 15° S. Further offshore, (10° W–0), the LLJ–low-CF relationship is weaker, while the AEJ-S–low-CF relationship is stronger, than closer to the coast. In tandem, the mid-tropospheric BC aerosol—low-CF relationship is also weaker near the coast than further offshore during both August 2017 and September 2016. For example, the Pearson correlation (r) for 600 hPa BC—low-CF north of 15° S in September 2016 is 0.56 offshore (10° W–0, 5-15° S, $p < 0.05$) and 0.35 near the coast (0–10° E, 5-15° S, $p < 0.05$). The mid-tropospheric BC—low-CF correlation is highest in September 2016 and lowest in October 2018, while the boundary layer BC–low-CF correlation is generally low and statistically insignificant for all three months, and occasionally negatively correlated (not shown).

5. Summary and discussion

This Part 2 of the meteorological overview paper describes the daily-resolved and synoptic variability in meteorological factors controlling aerosol transport and low cloud during the August, September, and October 2016–2018 deployments of ObsErvation of Aerosols above CLouds and their intEractionS (ORACLES) project. The key synoptic-scale meteorological characteristics that affect aerosol transport during each deployment month are summarized and illustrated in Fig. 18.
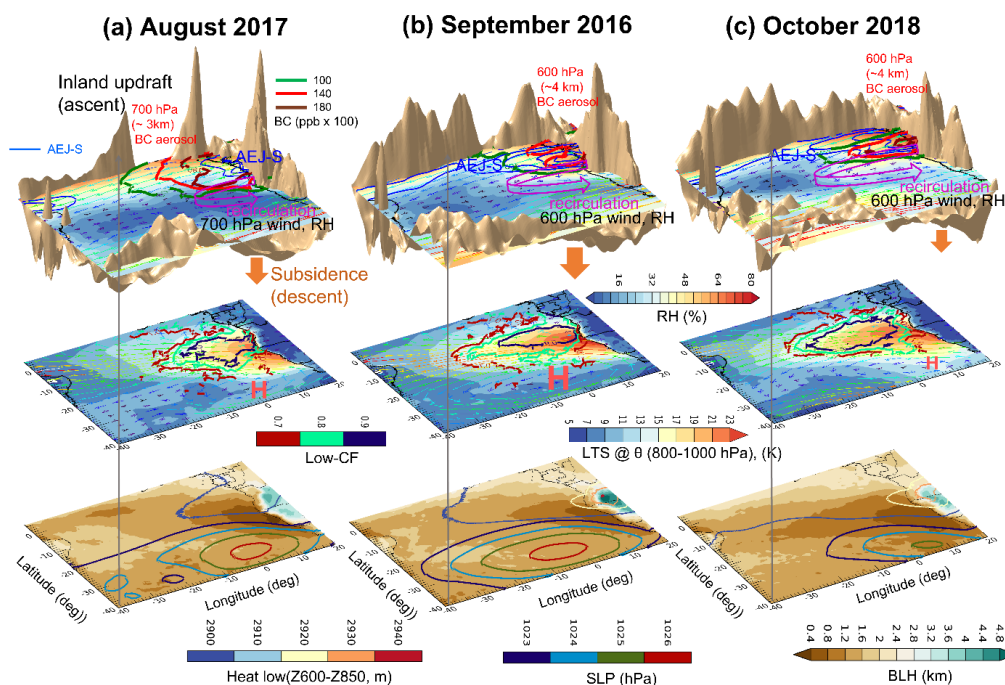
Figure 18. Visualization of (*top panels*) map of 700 hPa RH (shading, %), 700 hPa horizontal wind (vector, m s⁻¹), and 700 hPa BC aerosols (color lines, ppb x 100) for August 2017 and the same variables except for 600 hPa in September 2016 and October 2018. The 800 hPa vertical velocity for all months (gold bumpy surface, ω multiplied by -1 (i.e. - ω), hPa day⁻¹; above the RH contour plane is updraft and below the RH contour plane is subsidence). (*Middle panels*) map of LTS (shading, K) overlaid by 925 hPa horizontal wind (vector, m s⁻¹) and low-CF (color contours, 0.7–0.9 %). (*Bottom panels*) map of BLH (color shading, km) overlaid by thickness between 600 hPa and 850hPa (color contours, m) and sea level pressure (SLP; color contours, hPa) during (a) August 2017, (b) September 2016, and (c) October 2018. The magenta arrow in the top panels represents the recirculating flow to the African continent. The red "H" mark in mid panels refers to the anticyclones associated with St. Helena High.

- **Deployment 1 (September 2016):** September 2016 is characterized by a strong southern African easterly jet (AEJ-S) around 10° S, ~ 4 km (i.e., 600– 650 hPa) after 8 September. Black carbon (BC) aerosols and relative humidity (RH) are transported toward the ocean by the AEJ-S (top panel of Fig. 18b). Aerosol is occasionally present within the boundary layer in the CAMS reanalysis, though this is likely overestimated compared to observations (Shinozuka et al., 2022; Doherty et al., 2022). Daily-mean low tropospheric stability (LTS) is positively correlated with daily-

mean low-cloud fraction (low-CF; middle panel of Fig. 18b). High low-CF tends to be associated with low boundary layer height (BLH). The St. Helena High extended widely over the South Atlantic (bottom panel of Fig. 18b).

- o **In early September 2016 (1-9 Sept.):** A strong mid/upper-level mid-latitude trough intrusion (4 Sept.), and cut-off low over 20W-5°E, 15-30°S (2 Sept) strengthened the LLJ and southward mid-level flows near the coast. The St. Helena High extended over (30° W-20° E, 20-45° S) during this period.
- o **In mid-September (10–18 Sept.)**: Moist plumes originating from land and advected by the AEJ-S were associated with moist convection in the north (5–10° S) and dry convection in the south (15-25° S). A mid-latitude trough intrusion strengthened the LLJ and southward mid-level flows near the coast, forming a local anticyclone south of 20° S on 10 and 12 Sept. The BLH was elevated and disturbed, largely due to strong northward flow within the boundary layer associated with developing mid-latitude frontal system on 14-16 Sept. The boundary layer BC aerosol decreased over flight region on 18 Sept.
- o **In late September (19–30 Sept.)**: Moisture advected quickly as the AEJ-S developed and the LLJ also strengthened. The BLH was low over land and the coastal region (0-20° E, 15-30° S) on 20 Sept. Thereafter, a strong mid-latitude disturbance with a pronounced upper-level trough-ridge pattern developed over the central Atlantic, increasing SLP near the coast. The mid-latitude frontal system affected the southern region (0-10° E, 15-25° S), changing both the lower- and mid-level wind speed and direction, reducing the subsidence, and increasing the BLH at the end of the month.

- **Deployment 2 (August 2017)** – The AEJ-S became established after mid-August of 2017 as the southern hemisphere (SH) moved from its winter towards its spring, but mostly at a lower altitude (~ 3 km, ~700 hPa) and further north (5–7° S) compared to September, with another easterly jet aloft above 600-500 hPa (> 4 km). BC covaried with RH and the AEJ-S in 0-10° E, 5-15° S region around 3 km (~ 700 hPa) (top panel of Fig. 18a). The heat low was weaker than in September 2016. Low-CF was positively correlated with LTS, and particularly high over the southern flight region (middle panel of Fig. 18a). The high SLP is weaker than in September 2016 (bottom panel of Fig. 18a).
  - o **In early August ((5–13 Aug)**: Slow and unorganized moisture advection reflected a relatively slow-moving and weak AEJ-S. Strong mid to upper-level easterly jet strengthened (> 4 km) on 12 and 13 Aug. The St. Helena High persisted over the south Atlantic. Strong southwesterly wind associated with cut-off low over the 30-10° W, 20-40° S intensified the mid-level wind on 12 Aug.
  - o **In mid-August (14-21 Aug.)**: A suppressed AEJ-S and dry free troposphere persisted over the SE Atlantic. A strong mid to upper tropospheric easterly jet prevailed above 500 hPa over 5-15° S, 0-10° E. The AEJ-S thereafter developed around 20-21 Aug. Strong anticyclone and high SLP, very weak zonal winds, and intense northward meridional winds developed over the southern African coast throughout the vertical layer (600–925 hPa level) on 20–21 August 2017 as the mid-latitude trough amplified and pushed

northward. BLH was elevated over the 0-10° E, 15-25° S on 18-19 Aug, and along the southern African coast on 21 Aug. These were associated with strong mid-level (600 hPa) westerly and southwesterly wind.

- **In late August, (22-31 Aug.)**: Moisture was advected by the emerging AEJ-S. A cut-off low developed to the west of the flight region (20° W-0, 20-30° S) with the SLP increasing south of 30° S, 10° W-20° E on 26 Aug. A mid-level/upper-level trough amplified, leading to southward winds over the SE Atlantic coastal region (0-10° E, 20-30° S) on 28 Aug. Thereafter relatively fast-moving moisture was ~~advection~~ advected by the AEJ-S on 30-31 Aug. BLH over the south Atlantic (20-30° S, 20° W-00°) was elevated north of the strong mid-latitude jet at 40° S on 30-31 Aug.

- **Deployment 3 (October 2018)** – October 2018 was characterized by a strong AEJ-S around 10° S, ~ 4 km, transporting aerosol up to mid-October but not thereafter. The AEJ-S slightly weakened as moist convection increased later in the month on 23 October. The impact of the mid-latitude frontal systems increased after the latter half of the month. BC also varied with AEJ-S and RH around 600 hPa around 8-10° S (top panel of Fig. 18c), but its transport was diminished by the weakening AEJ-S for the end of October. The low-CF was the highest among the three deployment months (middle panel of Fig. 18c). The correlations between LTS, BLH, and low-CF are the least significant of the deployment months. The AEJ-S – LLJ and the low-CF – LLJ correlations were significant in October 2018, apparently affected by a rapidly developing mid-latitude frontal system associated with upper-level disturbance over the SE Atlantic Ocean. High SLP is noticeably reduced and BLH is shallowest among the deployment months (bottom panel of Fig. 18c).

  - **In early October (1–10 Oct.)**: Fast-moving (~12.8 m s⁻¹) convection mostly from developing continental convection (< 5° N) m coincided with a strong AEJ-S. An extensive high St. Helena high pressure developed over the South Atlantic (30° W-20° E, 25-45° S) on 2-3 Oct, like September climatological conditions. The highest boundary layer BC aerosol was found in the early period of Oct.

  - **In mid-October (11–21 Oct.):** The AEJ-S and moisture transport persisted with some variability as the continental convection was intensified. Subsidence and large-scale anticyclone were weaker than in September 2016. The mid-latitude upper-level flows were tied to the intensification of the surface low to the west of flight region on 15 and 21 Oct.

  - **In late October (22 –28 Oct.):** Convection marched further south (< 20° S) over land. The AEJ-S weakened, together with a temperature reduction over land, and a weakening of both the latitudinal moisture and temperature gradient. BLH over land (coast) on 23 Oct. was noticeably lower (higher) compared to other flight days. Moisture transport occurred from land to ocean as the AEJ-S regained strength towards the end of the month.

765 This paper provides a meteorological context for interpreting the airborne measurements gathered during the three ORACLES deployments to support related studies focusing on the detailed investigation of the processes controlling stratocumulus decks, aerosol lifting, transport, and their interactions. The variability of the meteorological fields during each deployment is highly modulated at a daily to synoptic time scale, including in subsidence and dry/moist convection, superimposed on a seasonal trend towards a stronger heat low (August to September) before moist convection intrudes (September to October). Fast-

770 moving dynamic disturbance such as mid-latitude wave intrusion or frontal systems, will disrupt the relation between stratocumulus and climatological large-scale subsidence, LTS, BLH, and LLJ. One implication of this paper is to enable us to expect when the direct or indirect aerosol radiative effect is dominant. For example, when the AEJ-S is elevated high around 4 km, the aerosol can also be elevated above the cloud deck, which is well observed in September and October. In contrast, when the AEJ-S is less elevated (e.g., August), the lower transport altitudes make it easier for the aerosol to be in contact with

775 the cloudy boundary layer and mix into it, increasing the importance of the boundary layer aerosol indirect and semi-direct effects.

While we examined several large-scale meteorological factors tied to aerosol transport and stratocumulus decks, the detailed investigation of the processes controlling stratocumulus decks, aerosol lifting, and transport is beyond the scope of this study. Future studies can focus on specific scientific questions such as 1) the roles of mid-latitude circulations on the

780 aerosol transport and its boundary layer entrainment, 2) the impact of the continental mesoscale convective system (MCS) on the AEJ-S and the biomass burning (BB) aerosols, 3) further investigation of aerosol warming effect in the boundary layer by disentangling the meteorological factors from the aerosol-induced cloud-adjustment based on the model and airborne measurement, 4) the impact of the unusual-to-climatology meteorological conditions on low-cloud, aerosols, and their interactions at different time scale, 5) the influence of smoke-induced aerosol on cloud type and precipitation by adjusting

785 large-scale environmental conditions, 6) the causal relationship among aerosols, low-cloud, and other meteorological factors over the different ocean basins and geography.

~~This paper provides insights into the synoptic-scale meteorological factors affecting the aerosol transport and stratocumulus decks, supporting related studies focusing on the detailed investigation of the processes controlling stratocumulus decks, aerosol lifting, transport, and their interactions.~~

790 **Data availability**

The data in this analysis are based on open-source dataset. ERA 5 data are available from the Copernicus Climate Change Service (C3S) at https://cds.climate.copernicus.eu/ (Hersbach et al., 2020). The MODIS Aqua (Terra) Level 3 product is from https://doi.org/10.5067/MODIS/MYD08_M3.006 (Platnick et al., 2015a; https://doi.org/10.5067/MODIS/MYD08_M3.006, Platnick et al., 2015b). VIIRS daily Level 3 cloud data is from (https://ladsweb.modaps.eosdis.nasa.gov/missions-and-

795 measurements/products/CLDPROP_D3_VIIRS_SNPP). ECMWF CAMS global reanalysis monthly mean data are available from https://ads.atmosphere.copernicus.eu/cdsapp#!/dataset/cams-global-reanalysis-eac4-monthly?tab=overview(Inness et

al., 2019). The ORACLES P-3 flight track data can be obtained from NASA Earth Science Project Office (ESPO) archive at https://doi.org/10.5067/Suborbital/ORACLES/P3/2016_V2 (ORACLES Science Team, 2020a) for the 2016 data, https://doi.org/10.5067/Suborbital/ORACLES/P3/2017_V2 (ORACLES Science Team, 2020b) for the 2017 data, and https://doi.org/10.5067/Suborbital/ORACLES/P3/2018_V2 (ORACLES Science Team, 2020c) for the 2018 data, respectively.

Author contributions

RW and PZ envisioned the original ORACLES meteorological overview concept, and ~~RU,~~ JMR, RU, and LP designed the manuscript structure. IC provided the climatological mean and monthly mean MODIS low cloud data and assisted JMR to obtain the VIIRS daily mean cloud data product. LP and JMR developed the methodology of determining the decoupled cloud boundary layer height (BLH). JMR processed the data analysis and wrote the manuscript. JMR, LP, PZ, RW, and RU organized results and PZ, LP, and RW provided substantial feedback for further interpretation of the results. All authors provided input and edited the manuscript. JR, RW, and PZ made critical contributions to the ORACLES field campaigns, and LP and RU led the meteorological forecast briefing during the whole ORALCES field campaigns.

Competing interests

Paquita Zuidema is a guest editor for the ACP Special Issue: "ACP special issue: New observations and related modelling studies of the aerosol–cloud–climate system in the Southeast Atlantic and southern Africa regions". The rest of the authors declare that they have no conflict of interest.

Special issue statement

This article is part of the special issue "New observations and related modeling studies of the aerosol-cloud-climate system in the Southeast Atlantic and southern Africa regions (ACP/AMT inter-journal SI)". It is not associated with a conference.

Acknowledgments

The authors give sincere gratitude to all the ORACLES participants who make the project successful. We also thanks to Kristina Pistone for helpful discussion in interpreting CAMS aerosol data. ORACLES campaign was funded by NASA Earth Venture Suborbital-2 (NNH13ZDA001N-EVS2). We also appreciate two anonymous reviews for their helpful comments and suggestions.

Reference

Abel, S. J., Barrett, P. A., Zuidema, P., Zhang, J., Christensen, M., Peers, F., Taylor, J. W., Crawford, I., Bower, K. N., and Flynn, M.: Open cells exhibit weaker entrainment of free-tropospheric biomass burning aerosol into the south-east Atlantic boundary layer, Atmos. Chem. Phys., 20, 4059–4084, https://doi.org/10.5194/acp-20-4059-2020, 2020.

Adebiyi, A., Zuidema, P., and Abel, S.: The convolution of dynamics and moisture with the presence of shortwave absorbing aerosols over the southeast Atlantic. *J. Clim.*, 28, 1997-2024, doi: 10.1175/JCLI-D-14-00352.1, 2015.

Adebiyi, A. A., and Zuidema, P.: The role of the southern African easterly jet in modifying the southeast Atlantic aerosol and cloud environments. Q. J. R. Meteorol. Soc. 142: 1574–1589, doi:10.1002/qj.2765., 2016.

Adebiyi, A. A., and Zuidema, P.: Low Cloud Cover Sensitivity to Biomass-Burning Aerosols and Meteorology over the Southeast Atlantic. J. Climate, 31, 4329-4346, doi: 10.1175/JCLI-D-17-0406.1, 2018.

Adebiyi, A. A., Zuidema, P., Chang, I., ~~and~~ Burton, S. P. and Cairns, B.: Mid-level clouds are frequent above the southeast Atlantic stratocumulus clouds, Atmos. Chem. Phys., 20, 11025–11043, doi:10.5194/acp-2020-324., 2020.

Alduchov, O. A., and Eskridge, R. E., : Improved Magnus' form approximation of saturation vapor pressure. J. Appl. Meteor., 35, 601–609, 1996.

Andersen, H., Cermak, J., Fuchs, J., Knippertz, P., Gaetani, M., Quinting, J., Sippel, S., and Vogt, R.: Synoptic-scale controls of fog and low-cloud variability in the Namib Desert, Atmos. Chem. Phys., 20, 3415–3438, https://doi.org/10.5194/acp-20-3415-2020, 2020,

Christensen, M. W., Jones, W. K., and Stier, P.: Aerosols enhance cloud lifetime and brightness along the stratus-to-cumulus transition. Proceedings of the National Academy of Sciences,117, 17591-17598, doi:10.1073/pnas.1921231117, 2020.

Deaconu, L. T., Ferlay, N., Waquet, F., Peers, F., Thieuleux, F., and Goloub, P.: Satellite inference of water vapour and abovecloud aerosol combined effect on radiative budget and cloudtop processes in the southeastern Atlantic Ocean, Atmos. Chem. Phys., 19, 11613–11634, https://doi.org/10.5194/acp-19-116132019, 2019.

De Szoeke, S. P., Verlinden, K.L., Yuter, S. E., and Mechem, D. B.: The Time Scales of Variability of Marine Low Clouds. J. Climate, 29, 6463-6481, doi:10.1175/JCLI-D-15-0460.1, 2016.

Dobracki, A., P. Zuidema, S. Howell, P. Saide, S. Freitag, A. Aiken, S. Burton, A. Sedlacek, J. Redemann and R. Wood 2022: An attribution of the low single-scattering albedo of biomass-burning aerosol over the southeast Atlantic. *Atmos. Chem. Phys. Disc.*, doi:10.5194/acp-2022-501

Doherty, S. J., Saide, P. E., Zuidema, P., Shinozuka, Y., Ferrada, G. A., Gordon, H., Mallet, M., Meyer, K., Painemal, D., Howell, S. G., Freitag, S., Dobracki, A., Podolske, J. R., Burton, S. P., Ferrare, R. A., Howes, C., Nabat, P., Carmichael, G. R., da Silva, A., Pistone, K., Chang, I., Gao, L., Wood, R., and Redemann, J.: Modeled and observed properties related to the direct aerosol radiative effect of biomass burning aerosol over the southeastern Atlantic, Atmos. Chem. Phys., 22, 1–46, https://doi.org/10.5194/acp-22-1-2022, 2022.

Gordon, H., Field, P. R., Abel, S. J., Dalvi, M., Grosvenor, D. P., Hill, A. A., Johnson, B. T., Miltenberger, A. K., Yoshioka, M., and Carslaw, K. S.: Large simulated radiative effects of smoke in the south-east Atlantic, Atmos. Chem. Phys., 18, 15261–15289, https://doi.org/10.5194/acp-18-15261-2018, 2018.

Hegarty, J., Lewis J., McGrath-Spangler, E. L., Henderson, J., Scarino, A. J., Decola, P., Ferrare R., Hicks, M., Adams-Selin, R. D., and Welton, E. J.: Analysis of the Planetary Boundary Layer Height during DISCOVER-AQ Baltimore-Washington, D. C., with Lidar and High-Resolution WRF Modeling, J. Appl. Metero. Climatol., 2679 – 2696, 57, DOI: 10.1175/JAMC-D-18-0014.1, 2018.

Hersbach, H., Bell, B., Berrisford, P., Hirahara, S., Horányi, A., Muñoz-Sabater, J., Nicolas, J., Peubey, C., Radu, R., Schepers, D., Simmons, A., Soci, C., Abdalla, S., Abellan, X., Balsamo, G., Bechtold, P., Biavati, G., Bidlot, J., Bonavita, M., De Chiara, G., Dahlgren, P., Dee, D., Diamantakis, M., Dragani, R., Flemming, J., Forbes, R., Manuel, F., Geer, A., Haimberger, L., Healy, S., Hogan, R. J., Hólm, E., Janisková, M., Keeley, S., Laloyaux, P., Lopez, P., Lupu, C., Radnoti, G., De Rosnay, P., Rozum, I., Vamborg, F., Villaume, S., Thépaut, J.-N.: The ERA5 global reanalysis, Q. J. R. Meteorol. Soc., 146, 1999-2049, doi:10.1002/qj.3803, 2020.

Holton, J. R.: An Introduction to Dynamic Meteorology, Elsevier Academic Press, Fourth edition, 2004.

Hubanks, P., Platnick, S., Meyer, K., King, M., Ackerman, S., Holz, B., Heidinger, A., Li., Y., Frey, R., Walther, A., Dutcher, S., Veglio, P., Quinn, G., Botambekov, D., Wind, G., Amarasinghe, N., Wang, C., Marchant, B., Ramachandran, B.: L3 CLDPROP User Guide, Version 1.8, 10 October 2019.

Inness, A., Ades, M., Agustí-Panareda, A., Barré, J., Benedictow, A., Blechschmidt, A.-M., Dominguez, J. J., Engelen, R., Eskes, H., Flemming, J., Huijnen, V., Jones, L., Kipling, Z., Massart, S., Parrington, M., Peuch, V.-H., Razinger, M., Remy, S., Schulz, M., and Suttie, M.: The CAMS reanalysis of atmospheric composition, Atmos. Chem. Phys., 19, 3515–3556, https://doi.org/10.5194/acp-19-3515-2019, 2019.

875   Klein, S. A., and Hartmann, D. L.: The seasonal cycle of low stratiform clouds, J. Climate, 6, 1588-1606, 1993.

Kuete, G., Mba, W. P., and Washington, R.: African Easterly Jet South: Control, maintenance mechanisms and link with Southern subtropical waves, Climate Dynamics, 54, 1539-1552, doi: 10.1007/s00382-019-05072-w, 2020.

Liu, N., Zhou, S., Liu, C. Guo, J.: Synoptic circulation pattern and boundary layer structure associated with PM2.5 during wintertime haze pollution episodes in Shanghai, Atmospheric Research, 186-195, 228, https://doi.org/10.1016/j.atmosres.2019.06.001, 2019.

Mallet, M., Nabat, P., Zuidema, P., Redemann, J., Sayer, A. M., Stengel, M., Schmidt, S., Cochrane, S., Burton, S., Ferrare, R., Meyer, K., Saide, P., Jethva, H., Torres, O., Wood, R., Martin, D. S., Roehrig, R., Hsu, C., Formenti, P.: Simulation of the transport, vertical distribution, optical properties and radiative impact of smoke aerosols with the ALADIN regional climate model during the ORACLES-2016 and LASIC experiments, Atmos. Chem. Phys., 19, 4963 – 4990, doi:10.5194/acp-19-4963-2019, 2019.

Mallet, M., Solmon, F., Nabat, P., Elguindi, N., Waquet, F., Bouniol, D., Sayer, A. M., Meyer, K., Roehrig, R.,Michou, M., Zuidema,P., Flamant,C., Redemann, J., Formenti, P.: Direct and semi-direct radiative forcing of biomass-burning aerosols over the southeast Atlantic (SEA) and its sensitivity to absorbing properties: a regional climate modeling study, Atmos. Chem. Phys., 20, 13191-13216, doi:10.5194/acp-20-13191-2020, 2020.

NASA ER-2: https://www.nasa.gov/centers/armstrong/news/FactSheets/FS-046-DFRC.html#:~:text=The%20ER%2D2%20is%20a,65%2C000%20feet%20within%2020%20minutes, 2014, last access on 08/15/2022,

NASA P-3: https://airbornescience.nasa.gov/aircraft/P-3_Orion_-_WFF, 2022, last access on 08/15/2022, 2022.

895   Nicholson, S.: A low-level jet along the Benguela coast, an integral part of the Benguela current ecosystem, Climatic Change, 99: 613. doi:10.1007/s10584-009-9678-z, 2010.

Ohsawa, T., Ueda, H., Hayashi, T., Watanabe, A., and Matsumoto, J.: Diurnal variations of convective activity and rainfall in tropical Asia. J. Meteor. Soc. Japan, 79, 333- 352, https://doi.org/10.2151/jmsj.79.333, 2001.

ORACLES Science Team: Moffett Field, CA, NASA Ames Earth Science Project Office (ESPO) [data set], https://doi.org/10.5067/Suborbital/ORACLES/P3/2016_V2, 2020a.

ORACLES Science Team: Moffett Field, CA, NASA Ames Earth Science Project Office (ESPO) [data set], https://doi.org/10.5067/Suborbital/ORACLES/P3/2017_V2, 2020b.

ORACLES Science Team: Moffett Field, CA, NASA Ames Earth Science Project Office (ESPO) [data set], https://doi.org/10.5067/Suborbital/ORACLES/P3/2018_V2, 2020c.

905 Pennypacker, S., Diamond, M., & Wood, R.: Ultra-clean and smoky marine boundary layers frequently occur in the same season over the southeast Atlantic. Atmospheric Chemistry and Physics, 20(4), 2341–2351. https://doi.org/10.5194/acp-20-2341-2020., 2020.

Pistone, K., Zuidema, P., Wood, R., Diamond, M., da Silva Arlindo M., Ferrada, G., Saide, P. E., Ueyama, R., Ryoo, J.-M., Pfister, L., Podolske, J., Noone, D., Bennett, R., Stith, E., Carmichael, G., Redemann, J., Flynn, C., LeBlanc, S., Segal-
910 Rozenhaimer, M., and Shinozuka, Y.: Exploring the elevated water vapor signal associated with the free tropospheric biomass burning plume over the southeast Atlantic Ocean, Atmos. Chem. Phys., 21, 9643–9668, 2021, https://doi.org/10.5194/acp-21-9643-2021, 2021.

Platnick, S., Hubanks, P., Meyer, K., and King, M. D.: MODIS Atmosphere L3 Monthly Product (08_L3). NASA MODIS Adaptive Processing System, (Terra), Goddard Space Flight Center [data set],
915 https://doi.org/10.5067/MODIS/MYD08_M3.006, 2015a.

Platnick, S., Hubanks, P., Meyer, K., and King, M. D.: MODIS Atmosphere L3 Monthly Product (08_L3). NASA MODIS Adaptive Processing System, (Aqua), Goddard Space Flight Center [data set], https://doi.org/10.5067/MODIS/MYD08_M3.006, 2015b.

Redemann, J., Wood, R., Zuidema, P., Doherty, S.J., Luna, B., LeBlanc, S.E., Diamond, M. S., Shinozuka, Y., Chang, I. Y.,
920 Ueyama, R., Pfister, L., Ryoo, J.-M., Dobracki, A. N., Da Silva, A. M., Longo, K. M., Kacenelenbogen, M. S., Flynn, C. J., Pistone, K., Knox, N. M., Piketh, S. J., Haywood, J. M., Formenti, P., Mallet, M., Stier, P., Ackerman, A.S., Bauer, S. E., Fridlind, A.M., Carmichael, G.R., Saide, P.E., Ferrada, G. A., Howell, S. G., Freitag, S., Cairns, B., Holben, B.N., Knobelspiesse, K.D., Tanelli, S., L'Ecuyer, T.S., Dzambo, A.M., Sy, O. O., McFarquhar, G. M., Poellot, M. R., Gupta, S., O'Brien, J. R., Nenes, A., Kacarab, M. E., Wong, J. P. S., Small-Griswold, J.D., Thornhill, K. L.,
925 Noone, D., Podolske, J. R., Schmidt, K.S., Pilewskie, P., Chen, H., Cochrane, S. P., Sedlacek, A. J., Lang, T.J., Stith, E., Segal-Rozenhaimer, M., Ferrare, R.A., Burton, S.P., Hostetler, C.A., Diner, D.J., Platnick, S.E., Myers, J.S., Meyer, K.G., Spangenberg, D.A., Maring, H., and Gao, L.: An overview of the ORACLES (ObseRvations of Aerosols above CLouds and their intEractionS) project: Aerosol-cloud-radiation interactions in the Southeast Atlantic basin. Atmos. Chem. Phys., 21, 1507–1563, 2021, doi:10.5194/acp-21-1507-2021, 2021.

930 Richter, I., Mechoso, C. R.: Orographic Influences on Subtropical Stratocumulus, J. Atmos. Sci., 63, 2585-2601, 2006.

Ryoo, J.-M., Pfister, L., Ueyama, R., Zuidema, P., Wood, R., Chang, I., and Redemann, J.: A meteorological overview of the ORACLES (ObseRvations of Aerosols above CLouds and their intEractionS) campaign over the southeastern Atlantic during 2016–2018: Part 1 – Climatology, Atmos. Chem. Phys., 21, 16689–16707, https://doi.org/10.5194/acp-21-16689-2021, 2021.

935 Sakaeda, N., Wood, R., and Rasch, P. J.: Direct and semidirect aerosol effects of southern African biomass burning aerosol. J. of Geophys. Res., 116(D12), doi: 10.1029/2010JD015540, 2011.

Scott, R. C., Myers, T. A., Norris, J. R., Zelinka, M. D., Klein, S. A., Sun, M., and Doelling, D. R.: Observed Sensitivity of Low-Cloud Radiative Effects to Meteorological Perturbations over the Global Oceans, *Journal of Climate*, *33*(18), 7717-7734, 2020.

940 Shinozuka, Y., P. E. Saide, G. A. Ferrada, S. P. Burton, R. Rerrare, S. J. Doherty, H. Gordon, K. Longo, M. Mallet, Y. Feng, Q. Wang, Y. Cheng, A. Dobracki, S. Freitag, S. G. Howell, S. LeBlanc, C. Flynn, M. Segal-Rosenhaimer, K. Pistone, J. R. Podolske, E. J. Stith, J. R. Bennett, G. R. Carmichael, A. da Silva, R. Govindaraju, R. Leung, Y. Zhang, L. Pfister, J.-M. Ryoo, J. Redemann, R. Wood, and P. Zuidema: Modeling the smoky troposphere of the southeast Atlantic: a comparison to ORACLES airborne observations from September of 2016, Atmospheric Chemistry and Physics, 945 https://doi.org/10.5194/acp-2019-678, 2020.

Tao, W.-K., Chen, J.-P., Li, Z., Wang, C., and Zhang, C.: Impact of aerosols on convective clouds and precipitation, Rev. Geophys., 50, RG2001, doi:10.1029/2011RG000369, 2012.

Witthuhn, J., Hünerbein, A., and Deneke, H.: Evaluation of satellite-based aerosol datasets and the CAMS reanalysis over the ocean utilizing shipborne reference observations, Atmos. Meas. Tech., 13, 1387–1412, https://doi.org/10.5194/amt-950 13-1387-2020, 2020.

Wood, R. and Bretherton, C. S.: On the Relationship between Stratiform Low Cloud Cover and Lower-Tropospheric Stability, J. Climate, 19, 6425 – 6432, 2006.

Wood, R.: Review, Stratocumulus Clouds, Mon. Wea. Rev., 140, 2373-2423, doi: 10.1175/MWR-D-11-00121.1, 2012.

Wood, R.: Clouds and Fog, Stratus and Stratocumulus, Encyclopedia of Atmospheric Sciences (Second Edition), 2015.

955 Zhang, Y. Stevens, B., Medeiros, B., Ghil, M.: Low-Cloud Fraction, Lower-Tropospheric Stability, and Large-Scale Divergence, J. Climate, 22, 4827 -4844, doi:10.1175/2009JCLI2891.1, 2009.

Zhang, J., and Zuidema, P.: The diurnal cycle of the smoky marine boundary layer observed during August in the remote southeast Atlantic, Atmos. Chem. Phys., 19, 14493–14516, doi:10.5194/acp-19-14493-2019, 2019.

Zhang, J., and Zuidema, P.: Sunlight-absorbing aerosol amplifies the seasonal cycle in low cloud fraction over the southeastAtlantic: *Atmos. Chem. Phys.*, **21**, p. 11179-11199, doi:10.5194/acp-21-11179-2021, 2021.

Zuidema, P.: Convective Clouds over the Bay of Bengal, Mon. Wea. Rev. 131, 780-798, https://doi.org/10.1175/1520-0493(2003)131<0780:CCOTBO>2.0.CO;2, 2003.

Zuidema, P., Leon, D., Pazmany, A., and Cadeddu, M.: Aircraft millimeter-wave passive sensing of cloud liquid water and water vapor during VOCALS-REx, Atmos. Chem. Phys., 12, 355–369, https://doi.org/10.5194/acp-12-355-2012, 2012.

Zuidema, P., Redemann, J., Haywood, J., Wood, R., Piketh, S., Hipondoka, M., and Formenti, P.: Smoke and Clouds above the Southeast Atlantic, Upcoming Fields Campaigns Probe Absorbing Aerosol's Impact on Climate, NOWCAST, DOI:10.1175/BAMS-D-15-00082.1, 2016.

Zuidema, P., Sedlacek, A. J. III, Flynn, C., Springston, S.,Delgadillo, R., Zhang, J., Aiken, A. C., Koontz, A., Muradyan, P.: The Ascension Island boundary layer in the remote southeast Atlantic is often smoky. Geophysical Research Letters, 45, 4456–4465, doi:10.1002/2017GL076926, 2018.

Supplementary materials:

A meteorological overview of the ORACLES (ObseRvations of Aerosols above CLouds and their intEractionS) campaign over the southeast Atlantic during 2016-2018: Part 2 – daily and synoptic characteristics

Ju-Mee Ryoo[1,2], Leonhard Pfister[1], Rei Ueyama[1], Paquita Zuidema[3], Robert Wood[4], Ian Chang[5], Jens Redemann[5]

[1] Earth Science Division, NASA Ames Research Center, Moffett Field, CA, USA

[2] Science and Technology Corporation, Moffett Field, CA, USA

[3] Department of Atmospheric Sciences, Rosenstiel School, University of Miami, Miami, FL, USA

[4] Department of Atmospheric Sciences, University of Washington, Seattle, WA, USA

[5] School of Meteorology, University of Oklahoma, Norman, OK, USA

Correspondence to: Ju-Mee Ryoo (ju-mee.ryoo@nasa.gov)
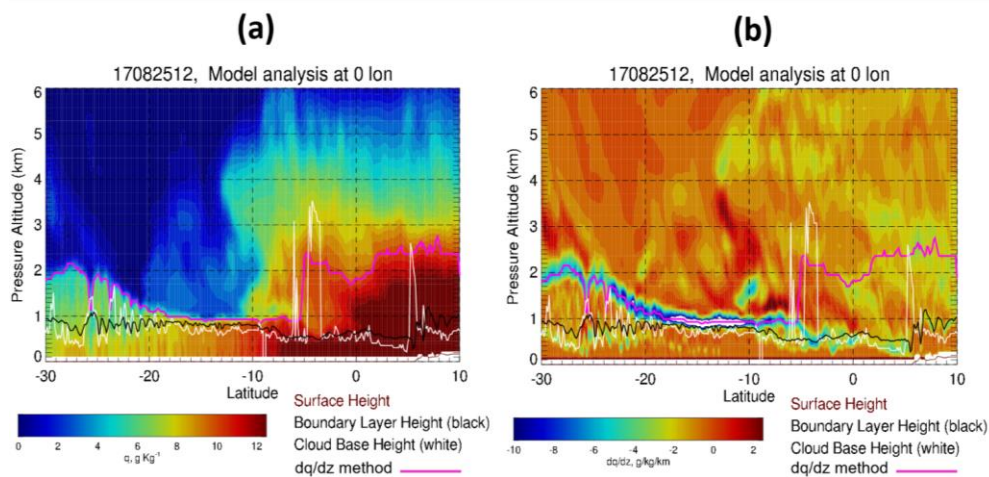
Figure S1. Map of (a) specific humidity (q, g kg^{-1}) and (b) vertical gradient of q (dq/dz, g kg^{-1} km^{-1}) overlaid by ERA5 boundary
25 **layer height (BLH) (Richardson number method, black line) and decoupled cloud BLH developed in this study (dq/dz method,**
magenta line) at 12:00 UTC 25 August 2017. Note that ERA5 BLH is referred to "Bulk Richardson number method" because it is
estimated using bulk Richardson number (ERA5 data description document). The surface height (brown line) and cloud base
height (white line) are also plotted.

30 **Note**: The plots demonstrate that 1) the bulk Richardson number method (black line) and the maximum vertical
gradient of q (dq/dz method; the detail methodology is shown in section 2.2 in the main manuscript) agree well
over the SE Atlantic Ocean 5–20° S at 0° E, but 2) it (black line) underestimates BLH over the convective (moist)
region (q> 10g kg^{-1}) and most of the ocean except for 5–20° S at 0° E compared to the dq/dz method. ECMWF
model-level data is shown here, but similar results are obtained using the pressure level data.
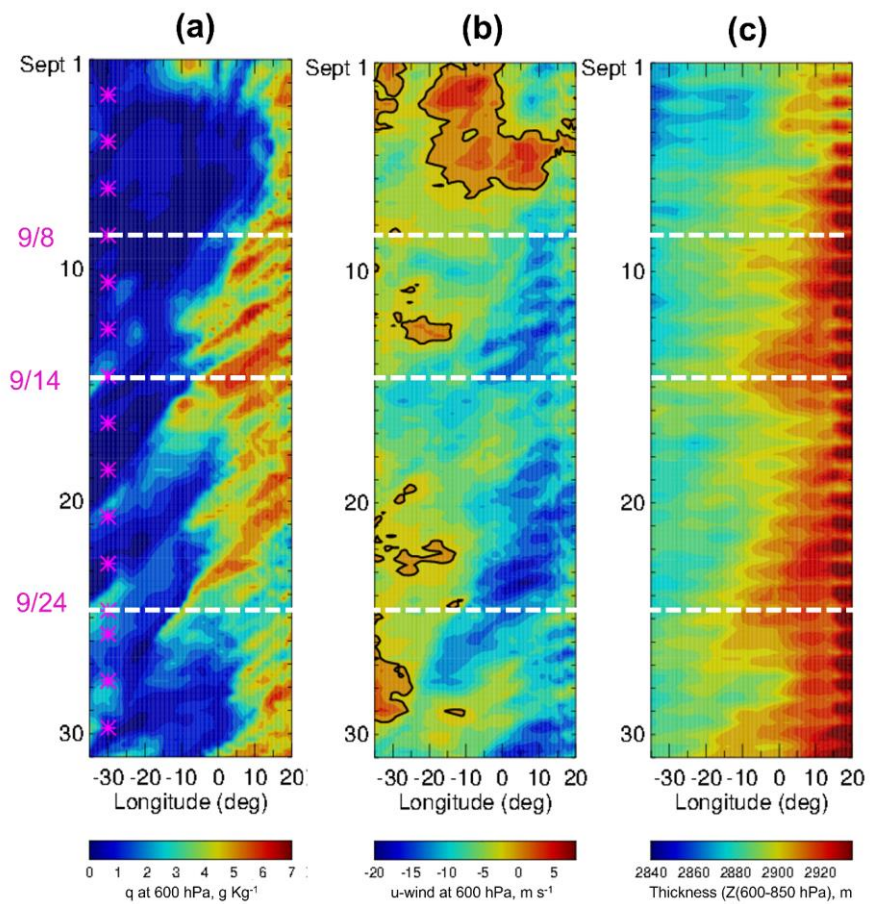
40   **Figure S2. (a-c) Longitude-time cross-section of 6 hourly (a) 600 hPa specific humidity (q, g kg^{-1}), (b) 600 hPa zonal wind (shading, m s^{-1}), (c) thickness (geopotential height difference (600-850 hPa); high values over a South African plateau represents the heat low, m) averaged over 8-10° S during September 2016. The ~~white~~ dashed white lines indicate the flight days investigated further in this study, and the asterisks represent the flight days during September 2016 deployment. The black contour in (b) represents 0 value of zonal wind.**
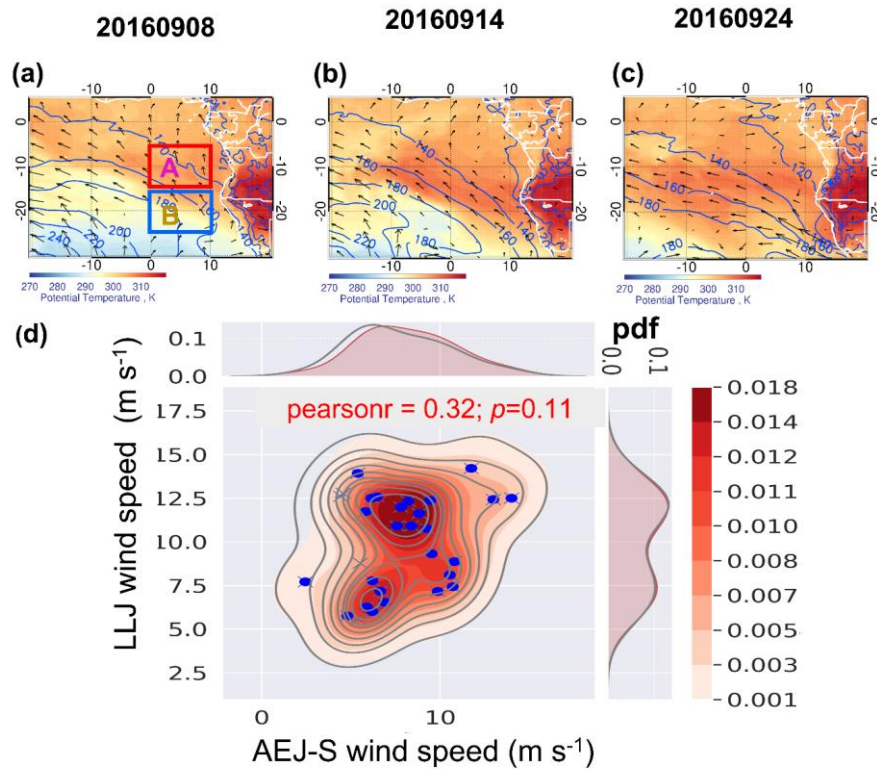
Figure S3. Map of (a–c) 850 hPa potential temperature (θ; shading, K) and 925 hPa horizontal winds (vectors, m s^{-1}) overlaid by 1000 hPa geopotential height (Z, blue contour, m) at 12:00 UTC 8, 14, and 24 September 2016. (d) 2-D joint pdf of the daily AEJ-S wind speed averaged over region A (0–10° E, 5–15° S) and LLJ wind speed averaged over region B (0–10° E, 15–25° S) marked in (a) (correlation is obtained for 5–30 September 2016 (blue dots) when the AEJ-S develops). The marginal plot shows their normalized pdf for the whole month (gray) and the days during the month when AEJ-S develops (red), respectively. The pearsonr in (h) refers to Pearson's correlation coefficient with its statistical significance (p-value).

Formatted: Font: Italic
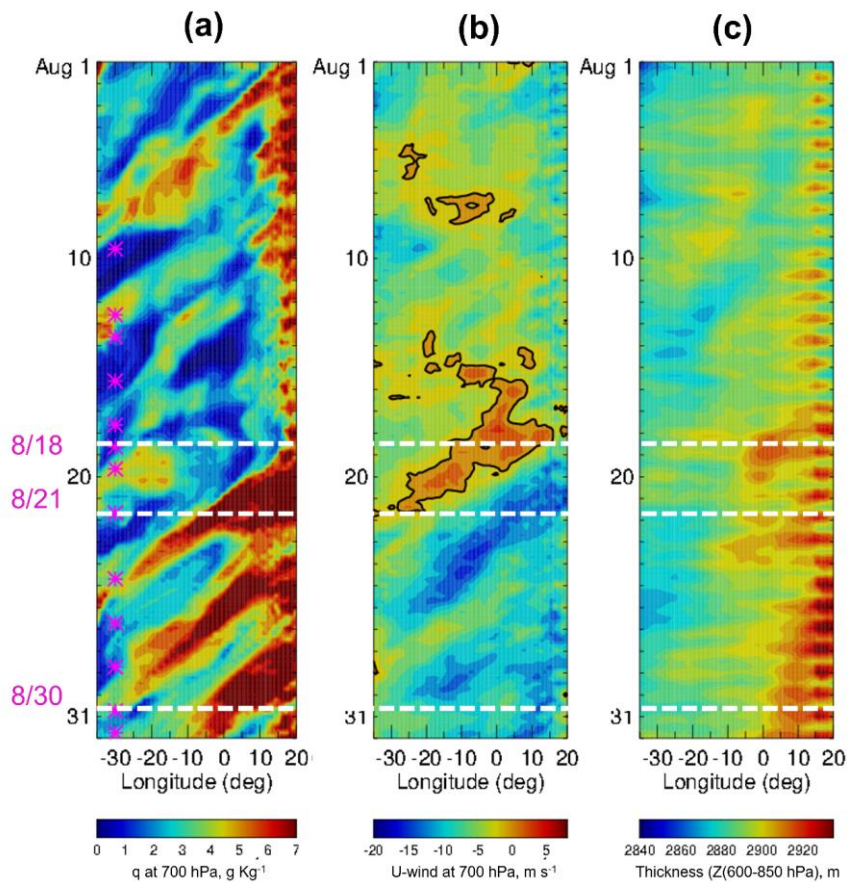
Figure S4. Longitude-time cross-section of 6 hourly (a) 700 hPa specific humidity (q, g kg^{-1}), (b) 700 hPa zonal wind (shading, m s^{-1}), (c) thickness (geopotential height difference (600-850 hPa); high values over a South African plateau represents the heat low, m) averaged over 5–7° S during August 2017. The ~~white~~ dashed white lines indicate the flight days investigated further in this study, and the asterisks represent the flight days during August 2017 deployment. The black contour in (b) represents 0 value of zonal wind.
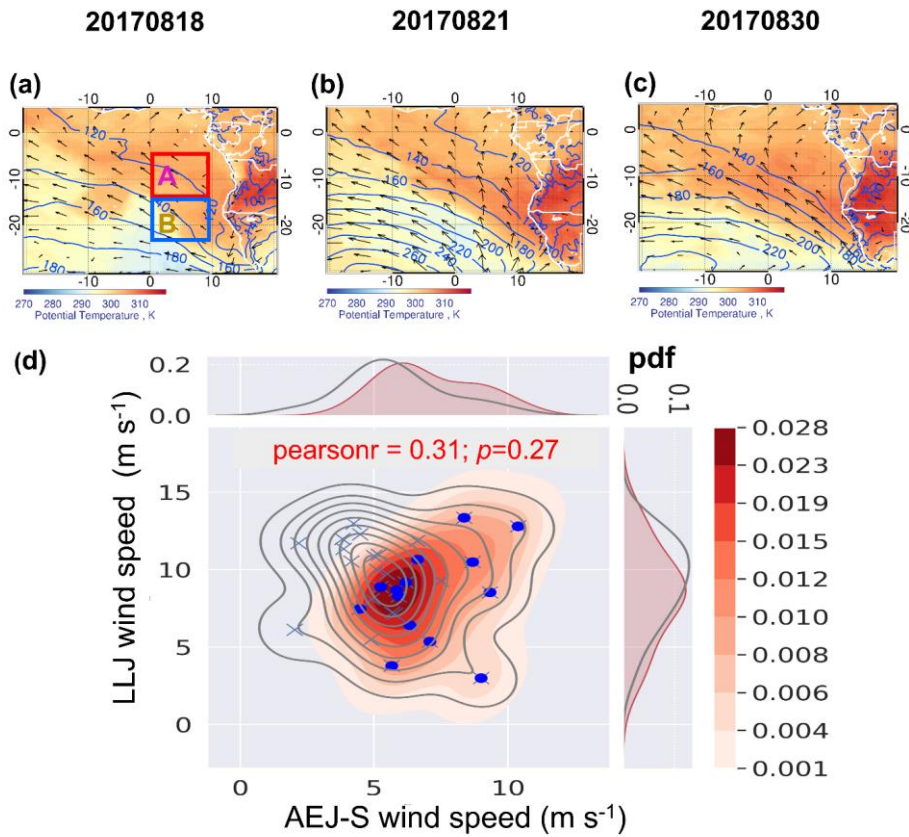
Figure S5. Map of (a–c) 850 hPa potential temperature (*θ*; shading, K) and 925 hPa horizontal winds (vectors, m s⁻¹) overlaid by 1000 hPa geopotential height (Z) (blue contour, m) at 12:00 UTC 18, 21, and 30 August 2017. (d) 2-D joint pdf of the daily AEJ-S wind speed averaged over region A (0–10° E, 5–15° S) and the LLJ wind speed averaged over region B (0–10° E, 15–25° S) marked in (a) (correlation is obtained for 18 – 31 August 2017 (blue dots) when the AEJ-S develops). The marginal plot shows their normalized pdf for the whole month (gray) and the days during the month when AEJ-S develops (red), respectively. The pearsonr in (h) refers to Pearson's correlation coefficient with its statistical significance (*p-value*).

Formatted: Font: Italic
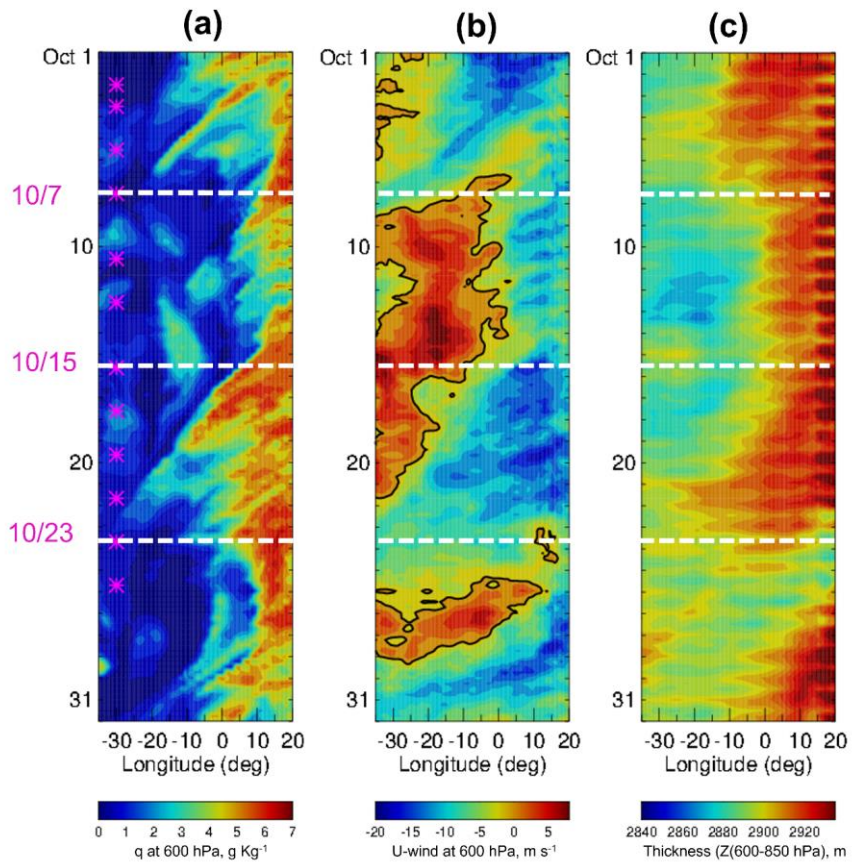
Figure S6. Longitude-time cross-section of 6 hourly (a) 600 hPa specific humidity (q, g kg^{-1}), (b) 600 hPa zonal wind (shading, m s^{-1}), (c) thickness (geopotential height difference (600-850 hPa); high values over a South African plateau represents the heat low, m) averaged over 8–10° S during October 2018. The ~~white~~ dashed white lines indicate the flight days investigated further in this study, and the asterisks represent the flight days during October 2018 deployment. The black contour in (b) represents 0 value of zonal wind.
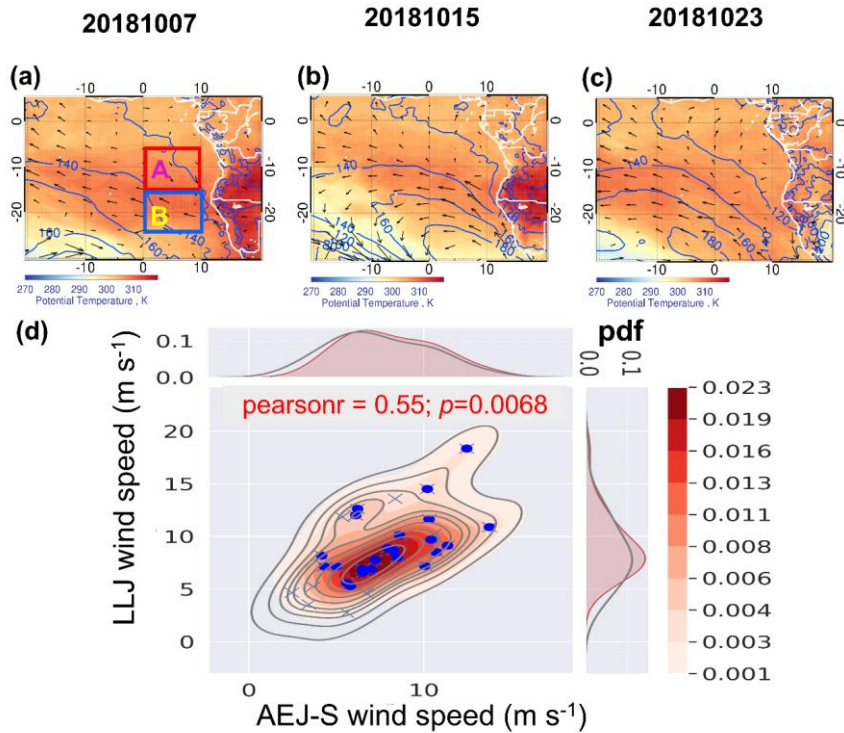
Figure S7. Map of (a–c) 850 hPa potential temperature (θ; shading, K) and 925 hPa horizontal winds (vectors, m s^{-1}) overlaid by 1000 hPa geopotential height (Z) (blue contour, m) at 12:00 UTC 7, 15, and 23 October 2018. (d) 2-D joint pdf of the daily AEJ-S

wind speed averaged over region A (0–10° E, 5–15° S) and the LLJ wind speed averaged over region B (0–10° E, 15–25° S) marked in (a) (correlation is obtained for 1–24 October 2018 (blue dots) when the AEJ-S develops). The marginal plot shows their normalized pdf for the whole month (gray) and the days during the month when AEJ-S develops (red), respectively. The pearsonr in (h) refers to Pearson's correlation coefficient with its statistical significance (*p-value*).

Formatted: Font: Italic

85
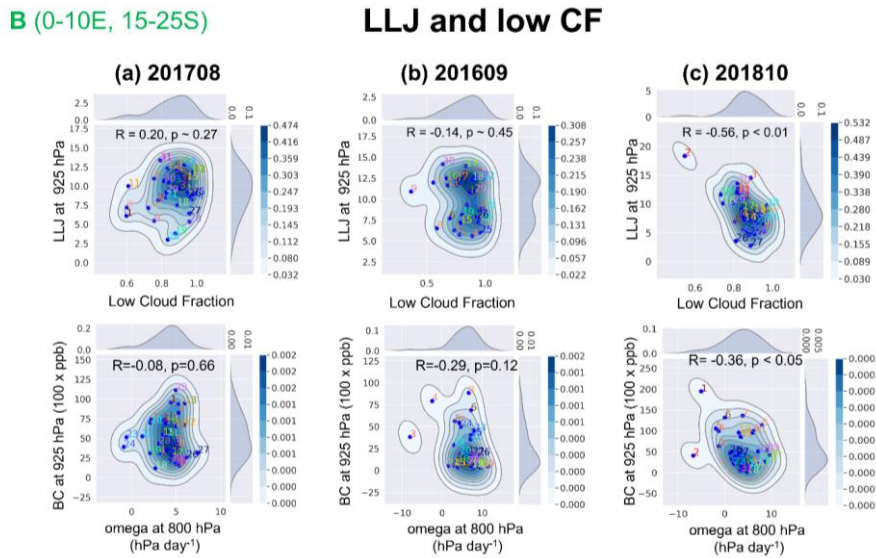
Figure S8. The 2-d density plot of (top) 925 hPa low-level jet (LLJ) and low-cloud fraction (low-CF) and (bottom) 925 hPa LLJ and 800 hPa vertical velocity (omega, positive value represents subsidence) during (a) August 2017, (b) September 2016, and (c) October 2018.
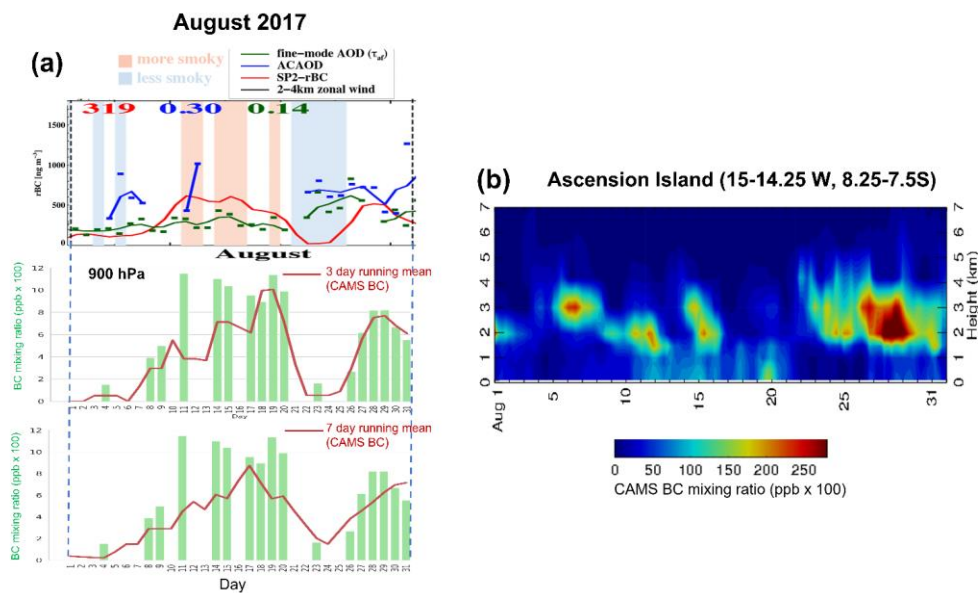
Figure S9. (a) (top) observed daily refractory BC (rBC) mass concentration over Ascension Island in August 2017, adapted from Zhang and Zuidema (2021). *Red line*: 3day running mean of the data. (Middle and bottom) 900 hPa CAMS BC (*red lines*: 3 day and 7 day running mean of daily averaged BC mixing ratio) over Ascension Island in August 2017. (b) Time-height cross section of BC averaged over Ascension Island (15W-14.25W, 8.25S-7.5S) in August 2017. The 1000 ng m^{-3} is equivalent to 1 ppb.
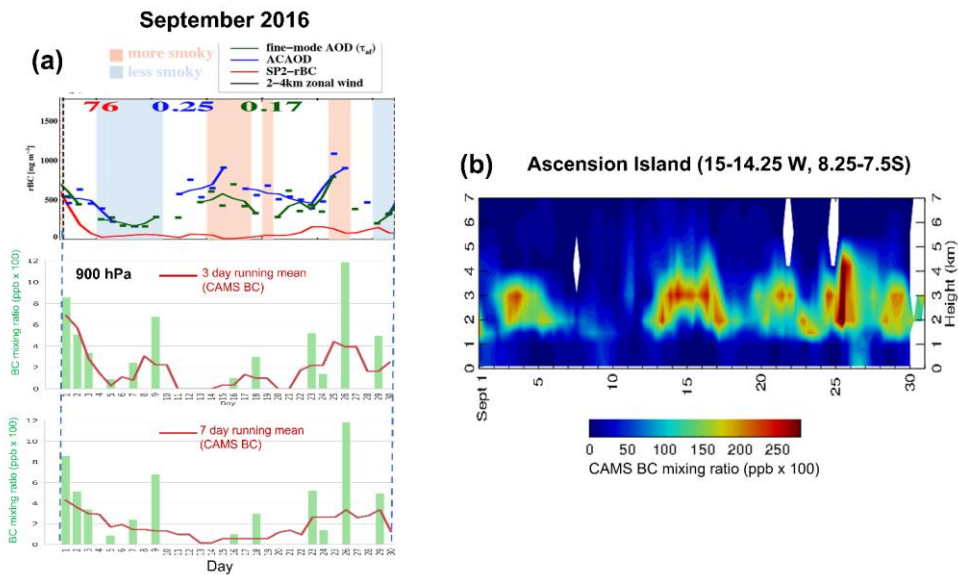
Figure S10. (a) (top) observed daily refractory BC (rBC) mass concentration over Ascension Island in September 2016, adapted from Zhang and Zuidema (2021). *Red line*: 3day running mean of the data. (Middle and bottom) 900 hPa CAMS BC (*red lines*: 3 day and 7 day running mean of daily averaged BC mixing ratio) over Ascension Island in September 2016. (b) Time-height cross section of BC averaged over Ascension Island (15° W-14.25° W, 8.25° S-7.5° S) in September 2016. The 1000 ng m^{-3} is equivalent to 1 ppb. The white area in (b) represents the missing values.
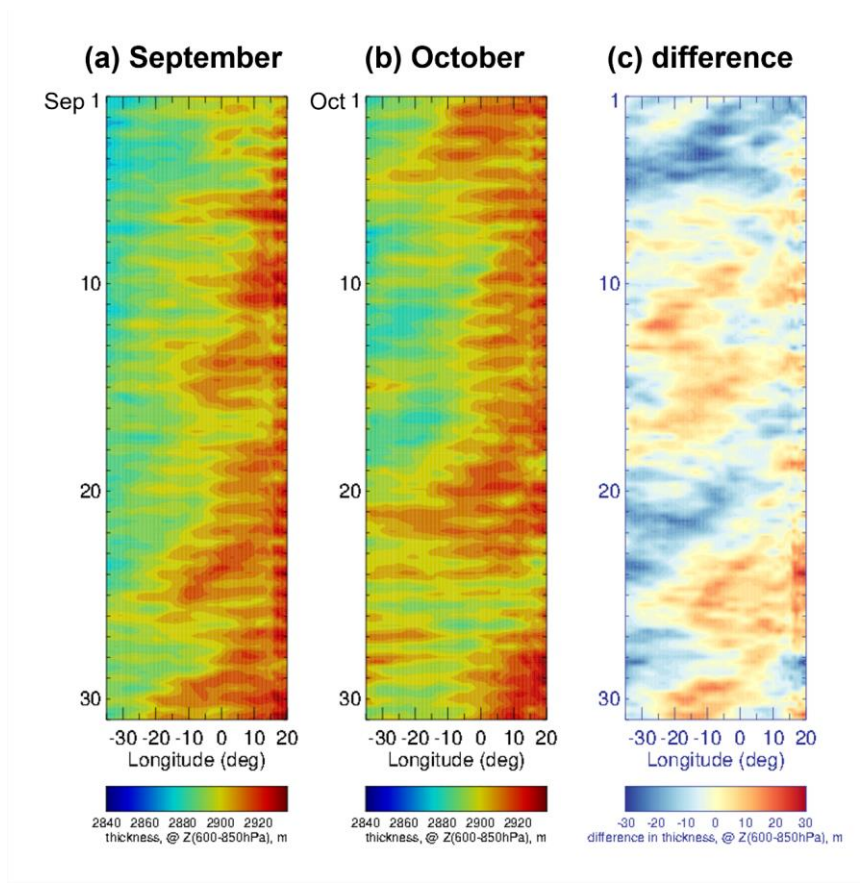
110

Figure S11. Longitude-time cross-section (Hovmöller diagram) of the 6-hourly thickness (geopotential height difference (600-850 hPa); high values over a South African plateau represents the heat low, m) averaged over 8-10° S during (a) September 2016, (b) October 2018, and (c) their difference. The red (blue) color in (c) represents the stronger (weaker) heat low in September 2016 than in October 2018.

115
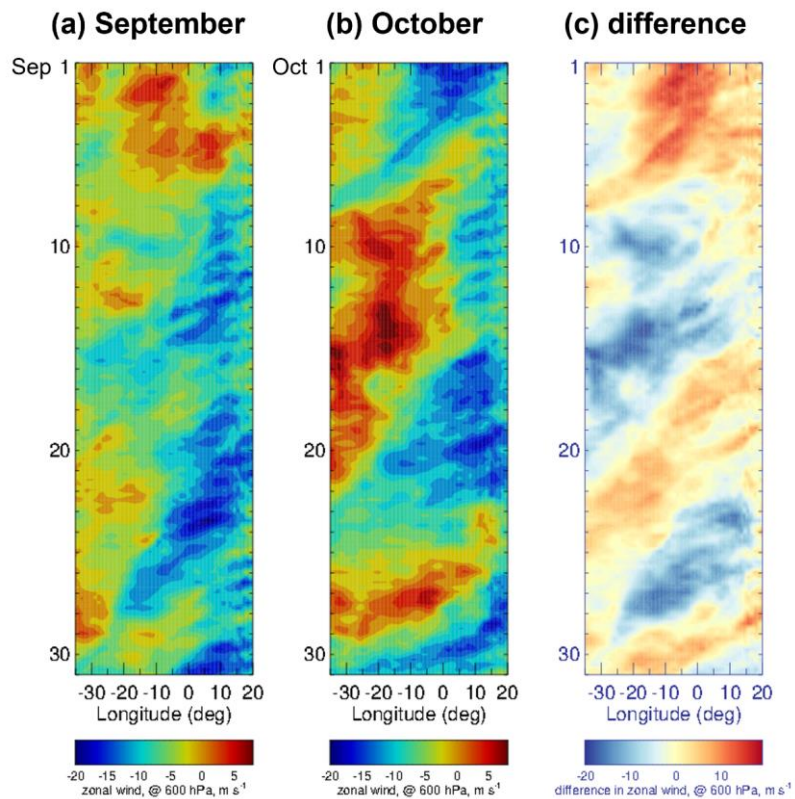
Figure S12. Longitude-time cross-section (Hovmöller diagram) of 6-hourly 600 hPa zonal wind (shading, m s^{-1}) averaged over 8-10° S during (a) September 2016, (b) October 2018, and (c) their difference. The red (blue) color in (c) represents the weaker (stronger) 600 hPa zonal easterly wind in September 2016 than in October 2018.

120

BLH, 600 hPa wind and geopotential, and SLP
September 2016 flight days
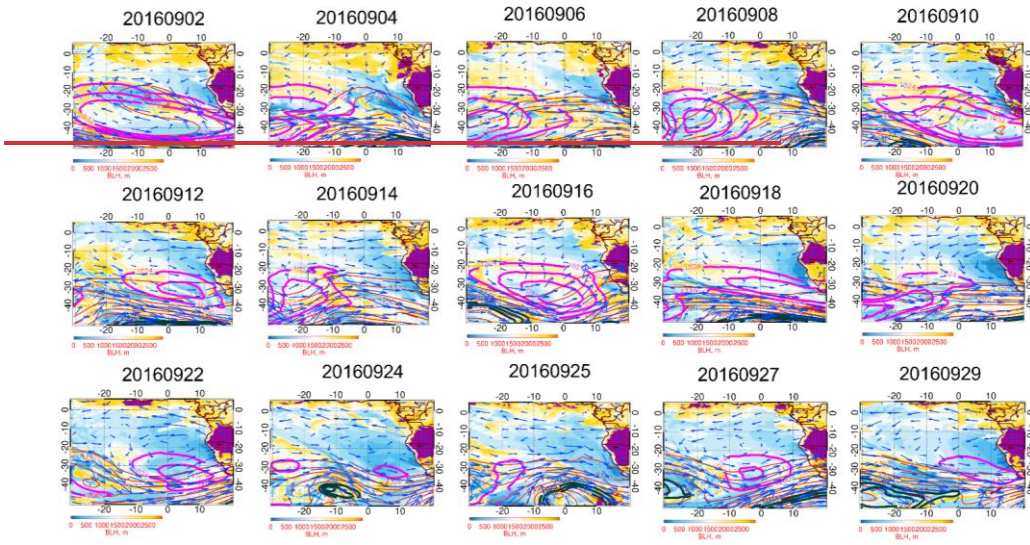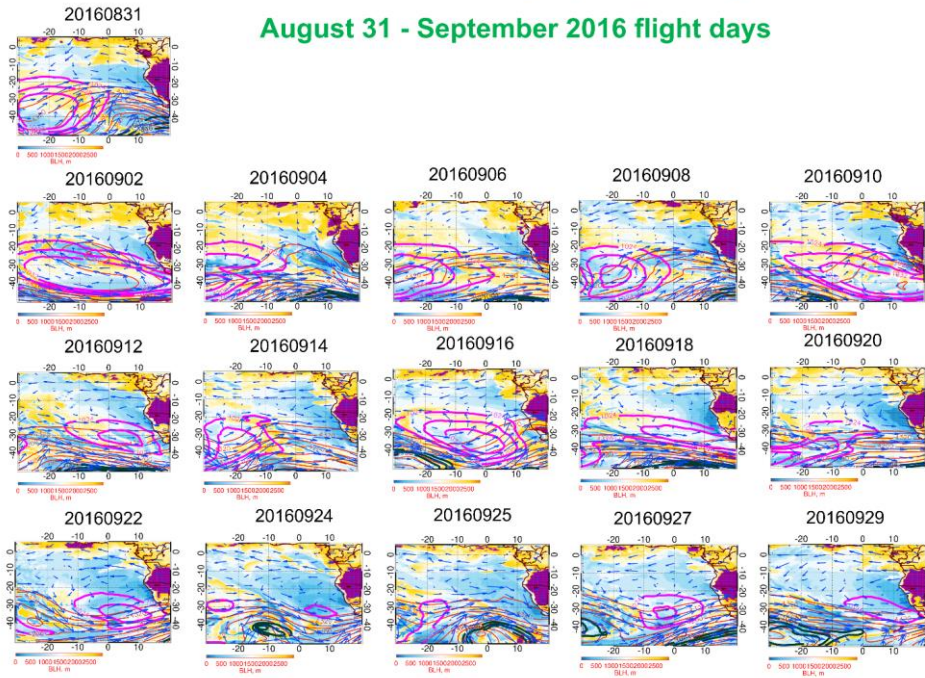
Figure S13. Map of BLH (shading, m) overlaid by 600 hPa horizontal winds (vectors, m s^{-1}), 600 hPa geopotential height (red lines, m), and sea level pressure (SLP; dark green (low-pressure: 996, 1000, 1004), and magenta (high-pressure: 1024, 1028, 1032), hPa) at 12:00 UTC on flight days on 31 August 2016 and<s>in</s> September 2016. The purple shading over the land refers to BLH higher than 3250 m.
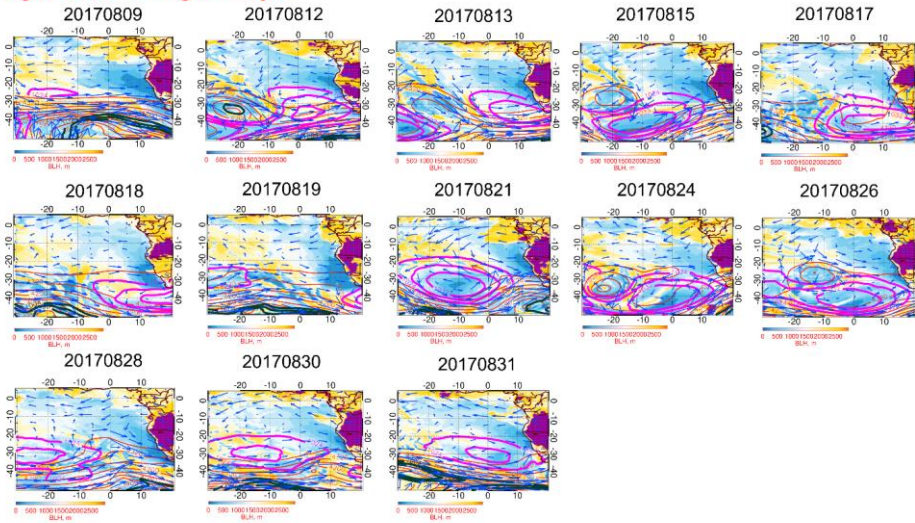
Figure S14. Map of BLH (shading, m) overlaid by 600 hPa horizontal winds (vectors, m s⁻¹), 600 hPa geopotential height (red lines, m), and sea level pressure (SLP; dark green (low-pressure: 996, 1000, 1004), and magenta (high-pressure: 1024, 1028, 1032), hPa) at 12:00 UTC on flight days in August 2017. The purple shading over the land refers to BLH higher than 3250 m.
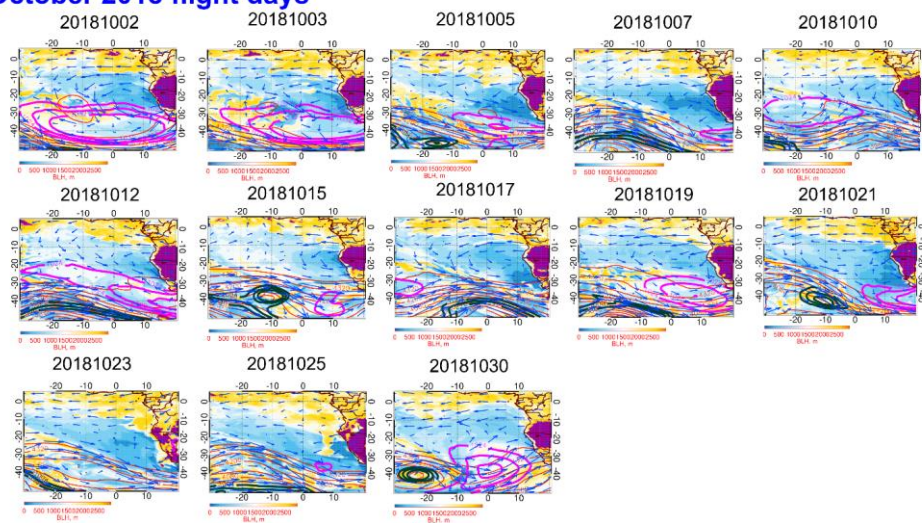
Figure S15. Map of BLH (shading, m) overlaid by 600 hPa horizontal winds (vectors, m s⁻¹), 600 hPa geopotential height (red lines, m), and sea level pressure (SLP; dark green (low-pressure: 996, 1000, 1004), and magenta (high-pressure: 1024, 1028, 1032), hPa) at 12:00 UTC on flight days in October 2018. The purple shading over the land refers to BLH higher than 3250 m.

135